

Spatial connectivity matches direction selectivity in visual cortex

<https://doi.org/10.1038/s41586-020-2894-4>

L. Federico Rossi¹✉, Kenneth D. Harris² & Matteo Carandini¹

Received: 29 January 2019

Accepted: 20 August 2020

Published online: 11 November 2020

 Check for updates

The selectivity of neuronal responses arises from the architecture of excitatory and inhibitory connections. In the primary visual cortex, the selectivity of a neuron in layer 2/3 for stimulus orientation and direction is thought to arise from intracortical inputs that are similarly selective^{1–8}. However, the excitatory inputs of a neuron can have diverse stimulus preferences^{1–4,6,7,9}, and inhibitory inputs can be promiscuous¹⁰ and unselective¹¹. Here we show that the excitatory and inhibitory intracortical connections to a layer 2/3 neuron accord with its selectivity by obeying precise spatial patterns. We used rabies tracing^{1,12} to label and functionally image the excitatory and inhibitory inputs to individual pyramidal neurons of layer 2/3 of the mouse visual cortex. Presynaptic excitatory neurons spanned layers 2/3 and 4 and were distributed coaxial to the preferred orientation of the postsynaptic neuron, favouring the region opposite to its preferred direction. By contrast, presynaptic inhibitory neurons resided within layer 2/3 and favoured locations near the postsynaptic neuron and ahead of its preferred direction. The direction selectivity of a postsynaptic neuron was unrelated to the selectivity of presynaptic neurons, but correlated with the spatial displacement between excitatory and inhibitory presynaptic ensembles. Similar asymmetric connectivity establishes direction selectivity in the retina^{13–17}. This suggests that this circuit motif might be canonical in sensory processing.

The selectivity of layer 2/3 (L2/3) neurons of the primary visual cortex (V1) for orientation and direction has unclear circuit origins. Selectivity is thought to emerge from the pooling of co-tuned layer 4 (L4) excitatory neurons¹⁸, amplified by excitatory connections between co-tuned L2/3 neurons^{1–6,8,9}. However, it remains unclear whether the inputs from L4 are tuned to the appropriate orientation¹, and whether they dominate or complement inputs from L2/3. Orientation tuning might be sharpened by inhibition^{19–21}, but the role of inhibition is controversial^{7,20–27} and inhibitory connections can be promiscuous¹⁰ and unspecific¹¹.

Moreover, none of these mechanisms explains direction selectivity, because the direction preference of L2/3 neurons often differs from their intracortical inputs¹. Direction selectivity might arise from tuned inhibition⁷ or from the spatial offset of excitation and inhibition²⁸, but these circuits have not yet been demonstrated. Spatial offsets between excitatory and inhibitory connectivity occur in the retina^{13–17} but have not been demonstrated in the cortex, where measurements *in vitro* are harder to relate to function^{20,29–32}.

Tracing inputs to a cortical neuron

To understand the circuits that determine the selectivity of individual L2/3 neurons, we established their intracortical presynaptic ensemble¹ (Fig. 1a, b). We used two types of transgenic mouse: *CaMK2a-GCaMP6* mice, which express the green calcium indicator GCaMP6 in cortical excitatory neurons, and *GAD2-NLS-mCherry* mice, which express the nuclear far-red marker NLS-mCherry in inhibitory neurons, with

GCaMP6 expressed virally in all neurons. In both lines, we electroporated 3–5 L2/3 pyramidal neurons with genes for the modified rabies receptor TVA, the rabies glycoprotein oG and the near-red marker dsRed (Fig. 1a, Extended Data Fig. 1). We then recorded visual responses in electroporated neurons (Fig. 1a), selected one neuron with robust responses and photo-ablated any additional neurons (Extended Data Fig. 2). We then injected a modified rabies virus¹² that could infect only the TVA-positive target neuron, and propagated to its presynaptic neurons to express dsRed (Fig. 1b). Finally, we used two-photon imaging to record from the postsynaptic neuron, its presynaptic ensemble and the surrounding population (10,000–14,000 neurons across layers) (Fig. 1b). For each postsynaptic neuron ($n = 17$), we identified 125 ± 23 (mean \pm s.e.m.) local presynaptic partners. We imaged daily, and confirmed that presynaptic neurons gave healthy responses for more than 12 days after injection (Extended Data Fig. 3).

Anatomy of presynaptic ensembles

We then classified the presynaptic neurons as excitatory or inhibitory (Fig. 1c–f). In *CaMK2a-GCaMP6* mice, we used somatic GCaMP6 fluorescence to classify presynaptic neurons as excitatory (Fig. 1c) or inhibitory (Fig. 1d, Extended Data Figs. 4, 5). In *GAD2-NLS-mCherry* mice, we used nuclear mCherry fluorescence to classify presynaptic neurons as inhibitory (Fig. 1f) or excitatory (Fig. 1e): because the emission spectra of dsRed and mCherry overlap, we separated their signals with multispectral imaging and spectral unmixing (Extended Data Fig. 6). On average, $63 \pm 13\%$ (mean \pm s.d., $n = 17$) of presynaptic

¹UCL Institute of Ophthalmology, University College London, London, UK. ²UCL Queen Square Institute of Neurology, University College London, London, UK. ✉e-mail: federico.rossi@ucl.ac.uk

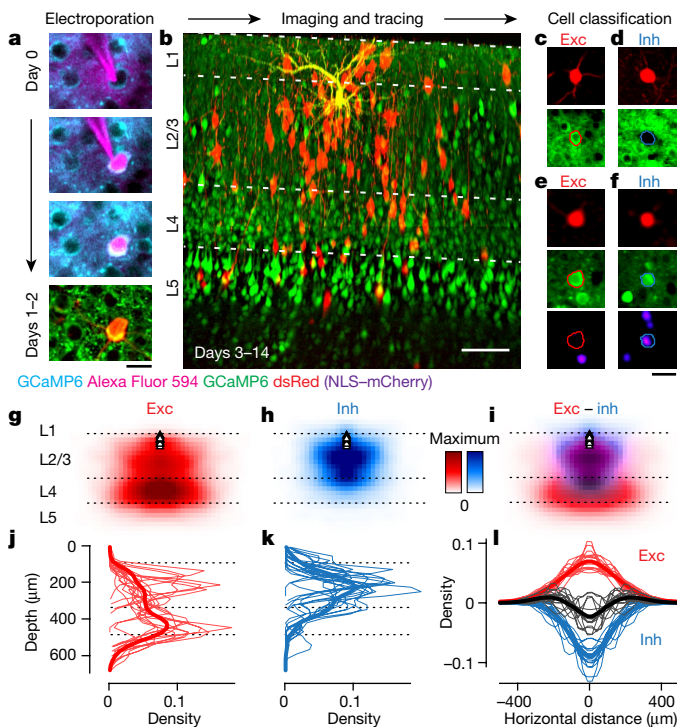


Fig. 1 | Tracing the excitatory and inhibitory presynaptic inputs to an L2/3 pyramidal neuron. **a**, Time lapse of electroporation (day 0) and dsRed expression (days 1–2) of the postsynaptic neuron. Scale bar, 20 μm . **b**, Montage of z-stack sagittal projections (taken 3 and 14 days after rabies injection), showing the postsynaptic neuron (yellow), its presynaptic ensemble (marked by dsRed, red) and the excitatory population (expressing GCaMP6 (green)). Lines indicate cortical layers. Scale bar, 100 μm . **c, d**, Examples of an excitatory (exc) ($n = 584$) and an inhibitory (inh) ($n = 426$) presynaptic neuron in a *CaMK2a-GCaMP6* mouse ($n = 13$): expression of dsRed (top) provides a somatic outline that matches the expression of GCaMP6 (bottom) for the excitatory neuron, but not for the inhibitory neuron. **e, f**, Examples of excitatory ($n = 373$) and inhibitory ($n = 117$) presynaptic neurons (top) in a *GAD-NLS-mCherry* mouse ($n = 4$) injected with *AAV-Syn-GCaMP6* (middle), in which nuclear mCherry (bottom) distinguishes inhibitory from excitatory neurons. Scale bar, 25 μm . **g**, Maximum normalized density of presynaptic excitation pooled across experiments ($n = 17$ postsynaptic neurons and 957 presynaptic neurons). All postsynaptic neurons resided in upper L2/3 (black triangles). **h**, As in **g**, for inhibition ($n = 543$ presynaptic neurons). **i**, Overlay of the maps of excitation and inhibition. Hue indicates the relative proportion of excitatory (red) and inhibitory (blue) inputs, and saturation indicates maximum normalized neuronal density. **j, k**, Depth distributions for excitatory and inhibitory presynaptic neurons, for individual experiments (thin curves), and pooled data (thick curve). Vertical scale as in **g–i**. **l**, As in **j, k**, for the radial distributions of excitatory (red) and inhibitory (blue) presynaptic neurons, and their difference (black). Horizontal scale as in **g–i**.

neurons were excitatory and this fraction converged towards 70% in experiments with the highest yield (Extended Data Fig. 4).

The excitatory and inhibitory ensembles that provided input to an L2/3 pyramidal cell followed markedly different laminar and horizontal distributions (Fig. 1g–l). Excitatory inputs were densest in L4 and spanned a large vertical and horizontal range (Fig. 1g, j). By contrast, inhibitory inputs dominated in L2/3 and clustered near the postsynaptic neuron (Fig. 1h, k). These differences in distribution were consistent across postsynaptic neurons (Fig. 1j–l, Extended Data Fig. 7). The broader horizontal distribution of excitatory relative to inhibitory inputs thus generated an inverse ‘Mexican hat’ profile, with inhibition dominating in proximal regions and excitation dominating in distal regions (Fig. 1i, l). These profiles of connectivity obtained in the intact brain were not apparent in previous measurements that were obtained *in vitro*^{29–31}.

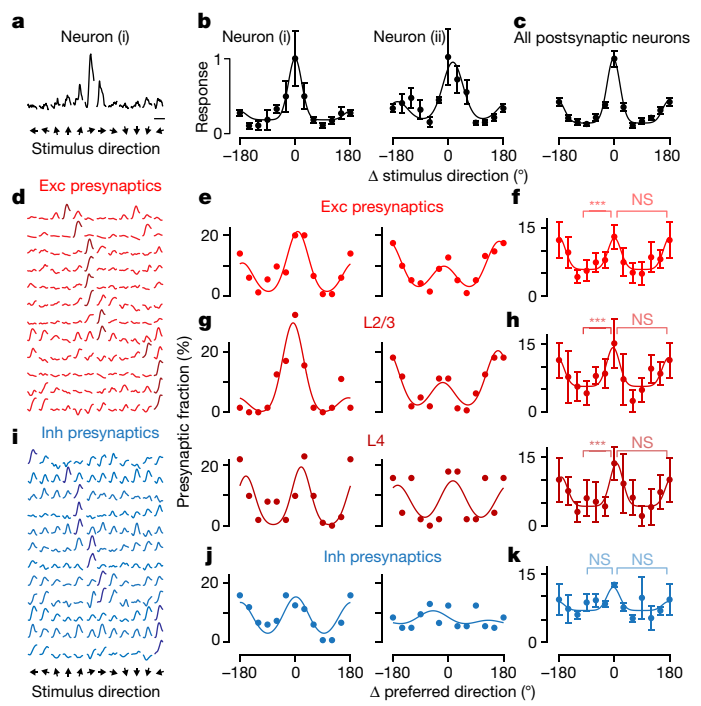


Fig. 2 | Excitatory and inhibitory presynaptic ensembles are co-tuned for orientation but not direction. **a**, Peak-normalized responses to drifting gratings of an example postsynaptic neuron. Scale bar, 5 s. **b**, Tuning curves of the postsynaptic neuron in **a** (neuron (i)) and of a second postsynaptic neuron (neuron (ii)), after alignment of their preferred direction to 0° (mean \pm s.e.m., $n = 10$ trials). Preferred directions for the two neurons were 30° and 180°. **c**, Average tuning across postsynaptic neurons responding to drifting gratings (mean \pm s.e.m., $n = 16$). **d**, Normalized responses of 12 example excitatory presynaptic neurons traced from the first postsynaptic neuron in **a**. **e**, Distribution of preferred direction from the excitatory presynaptic ensembles connected to the postsynaptic neurons in **b**, relative to the postsynaptic preferred direction. **f**, Average distribution of preferred direction for excitatory presynaptic neurons pooled across all layers ($n = 15$, median \pm m.a.d.). *** $P_{\text{KW}} = 10^{-8}$, one-way Kruskal–Wallis test across orientations; NS, $P_{\text{W}} = 0.39$, Wilcoxon signed-rank test between preferred and opposite direction. **g**, As in **e**, for presynaptic ensembles within L2/3 (top) and L4 (bottom). **h**, As in **f**, for presynaptic ensembles within L2/3 (top) ($n = 15$, $P_{\text{KW}} = 10^{-7}$, $P_{\text{W}} = 0.49$) and L4 (bottom) ($n = 13$, $P_{\text{KW}} = 2 \times 10^{-5}$, $P_{\text{W}} = 0.59$). **i**, As in **d**, for 12 example inhibitory presynaptic neurons. **j**, As in **e**, for the inhibitory presynaptic ensembles. **k**, As in **f**, for the average distribution of preferred direction of presynaptic inhibitory neurons ($n = 4$, $P_{\text{KW}} = 0.38$, $P_{\text{W}} = 0.25$).

Co-tuning for orientation but not for direction

Consistent with some^{2–4,8}—but not with other^{1,9}—previous observations, the orientation preference of the postsynaptic neuron strongly agreed with its excitatory presynaptic ensemble, regardless of layer (Fig. 2). In most experiments (16 out of 17) the postsynaptic neuron responded to gratings ($59 \pm 18\%$ (mean \pm s.d.), $n = 15$ datasets for which we recorded presynaptic responses) (Fig. 2a–c), so we could compare their preferences. Different presynaptic ensembles differed in their preferred orientation and direction (one-way Kruskal–Wallis test probability $P_{\text{KW}} = 10^{-7}$). The ensembles were prevalently tuned to the orientation preferred by the postsynaptic neuron (Fig. 2e, f) (circular correlation $r = 0.75$, probability $P_r = 4 \times 10^{-3}$, circular V test, probability $P_V = 10^{-7}$) (Extended Data Fig. 8). On average, more than twice as many presynaptic neurons preferred the postsynaptic preferred orientation over the orthogonal orientation. This co-tuning for orientation was prevalent not only in L2/3 (refs. ^{2,4}), but also in L4 ($P_{\text{KW}} = 10^{-7}$ and $P_{\text{KW}} = 10^{-4}$) (Fig. 2g, h, Extended Data Fig. 8).

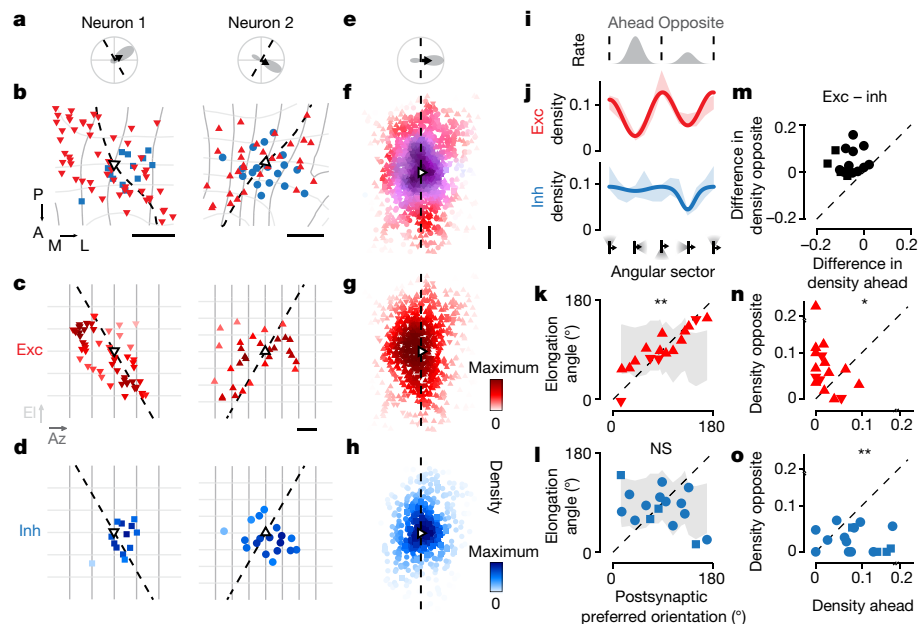


Fig. 3 | Elongated excitation and spatially offset inhibition accord with direction selectivity. **a**, Polar tuning curve of two postsynaptic neurons, showing preferred orientation (dashed) and direction (arrow). **b**, Excitatory (red) and inhibitory (blue) presynaptic ensembles of postsynaptic neuron (open triangle, pointing in the preferred direction). The postsynaptic preferred orientation maps to a curve in the cortex (dashed). Retinotopy is marked in 5° steps of azimuth (dark grey) and elevation (light grey). P, posterior; A, anterior; M, medial; L, lateral. Scale bars, 200 µm. **c**, Excitatory presynaptic neurons in **b** replotted in visual space. Saturation indicates density. Az, azimuth; El, elevation. Scale bar, 5°. **d**, As in **c**, for inhibitory presynaptic neurons. **e**, Average polar tuning curve across postsynaptic neurons, aligned to preferred direction ($n=16$). **f**, Excitatory and inhibitory presynaptic ensembles in visual space, pooled after alignment to the postsynaptic preferred direction ($n=16$). Hue indicates the relative proportion of excitation (red) and inhibition (blue); saturation indicates the average maximum normalized density. Scale bar, 5°. **g**, As in **f**, for excitatory presynaptic neurons. **h**, As in **f**, for inhibitory presynaptic neurons. **i**, Average postsynaptic tuning curve from **e**. **j**, Angular

density (shaded) ($\text{mean} \pm \text{s.e.m.}, n=16$) of excitatory (red) and inhibitory (blue) presynaptic neurons relative to the postsynaptic preferred direction. A sinusoid (capturing orientation selectivity) summed with a Gaussian (capturing direction selectivity) fit the data. **k**, The angle of elongation of the excitatory presynaptic ensemble correlates with the postsynaptic preferred orientation ($r=0.72, P_r=7 \times 10^{-3}$ and $P_v=10^{-4}, n=16$) significantly more than expected by chance (shaded area; median \pm m.a.d.) ($P_{r,\text{rand}}=10^{-3}$ and $P_{v,\text{rand}}<10^{-4}$). **l**, Conversely, the angle of elongation of the inhibitory presynaptic ensemble does not correlate with the postsynaptic preferred orientation ($r=-0.07, P_r=0.77$ and $P_v=0.12, n=16$). **m–o**, Comparison of density in sectors opposite and ahead of the postsynaptic preferred direction for excitation ($P_w=4 \times 10^{-2}, n=16$, two-sided Wilcoxon signed-rank test) (**n**), inhibition ($P_w=3 \times 10^{-3}$) (**o**), and the difference between excitation and inhibition ($P_w=4 \times 10^{-4}$) (**m**). In **b–o**, upward-pointing triangles and circles indicate *CaMK2α-GCaMP6* datasets; downward-pointing triangles and squares indicate *GAD2-NLS-mCherry* datasets.

Co-tuning for orientation did not result from local biases in preference^{33,34}: the presynaptic ensemble was significantly more co-tuned than the surrounding population (circular variance 0.71 ± 0.15 versus 0.85 ± 0.06 (median \pm median absolute deviation (m.a.d.)), Wilcoxon signed-rank test, probability $P_w=2 \times 10^{-3}, n=15$). Moreover, the alignment of this ensemble to the postsynaptic orientation was significantly greater than in neuronal ensembles selected at random, and hence could not be expected by chance (comparison between data and random circular correlation, probability $P_{r,\text{rand}}<10^{-4}$; comparison between data and random *V* statistic, probability $P_{v,\text{rand}}<10^{-4}$) (Extended Data Fig. 8).

By contrast, the presynaptic inhibitory ensemble was only weakly biased to the orientation preference of the postsynaptic neuron (Fig. 2i–k). Inhibitory neurons were more broadly tuned than excitatory ones (median orientation selectivity index 0.21 versus 0.43, $P=0.015$, two-sample Kolmogorov–Smirnov test) (Fig. 2i). The inhibitory presynaptic ensemble was somewhat biased towards the postsynaptic preferred orientation ($P_v=0.05, n=4$) (Fig. 2j, k, Extended Data Fig. 8), but characterized by a broader distribution of preferred orientations than the excitatory ensemble (circular variance 0.76 ± 0.16 versus 0.59 ± 0.21 (median \pm m.a.d.), $P_w=0.065, n=4$) (Fig. 2j, k), and not significantly different from random samples of nearby neurons (0.76 ± 0.16 versus 0.80 ± 0.10 (median \pm m.a.d.), $P_w=0.88, n=4$). Therefore, an L2/3 neuron integrates excitation from an ensemble strongly co-tuned for orientation, and inhibition from an ensemble with varied and weaker tuning.

Presynaptic ensembles showed no consistent co-tuning for stimulus direction (Fig. 2e–k, Extended Data Fig. 8). Some excitatory presynaptic ensembles comprised more neurons that were selective for the same direction as the postsynaptic neuron¹ (neuron (i) in Fig. 2e, g), but other ensembles favoured the opposite direction (neuron (ii) in Fig. 2e, g). On average, the number of presynaptic excitatory neurons that preferred the same direction as the postsynaptic neuron was not higher than the number that preferred the opposite direction ($P_w=0.39$) (Fig. 2f). Similar results were seen within L2/3 ($P_w=0.49$) or L4 ($P_w=0.59$) (Fig. 2h). Furthermore, the postsynaptic direction selectivity index was unrelated (Pearson correlation, $P_r=0.24$) to the selectivity of the excitatory presynaptic ensemble (the relative number of presynaptic neurons that prefer the postsynaptic direction versus the opposite one). Direction selectivity in L2/3 neurons therefore might not depend on the co-tuning of their synaptic inputs.

Directional spatial connectivity

We next compared the selectivity of the postsynaptic cells to the spatial patterns of their excitatory and inhibitory presynaptic ensembles (Fig. 3a, b). To characterize these patterns, we estimated retinotopy for every point in the cortex^{35,36} (Extended Data Fig. 9), and obtained maps that exhibited typical curvatures and anisotropies³⁷ (Fig. 3b).

The excitatory and inhibitory presynaptic ensembles exhibited spatial patterns and offsets that matched the tuning of the postsynaptic

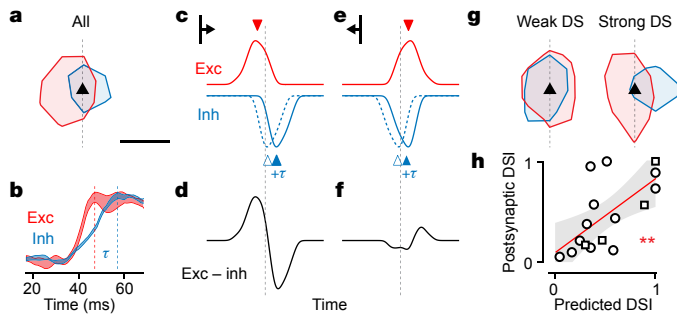


Fig. 4 | Spatially offset and delayed excitation and inhibition predict postsynaptic direction selectivity. **a**, Average excitatory and inhibitory presynaptic densities across experiments, showing contour at 10% of peak value. Scale bar, 5°. **b**, In response to a visual stimulus, inhibitory currents (blue) rise in L2/3 pyramidal neurons later than do excitatory currents (red). Traces indicate maximum normalized changes in synaptic conductance measured in the V1 of awake mice. This panel was adapted with permission from ref.³⁸. **c**, Simulated excitatory (red) and inhibitory (blue) presynaptic activity triggered by a bar sweeping in the postsynaptic preferred direction, as a function of time. The dotted line indicates the crossing of the bar with the position of the postsynaptic neuron (dashed line in **a**). Inhibitory activity is shown with the delay provided solely by spatial offset (dashed blue) and with the additional inhibitory lag ($+\tau$, solid blue). **d**, Net synaptic input (excitatory – inhibitory) to the postsynaptic neuron. **e, f**, As in **c, d**, for a bar sweeping opposite to the preferred direction. **g**, As in **a**, for densities averaged across the three postsynaptic neurons with weakest direction selectivity (DSI) (left) and for the three postsynaptic neurons with strongest direction selectivity (right). **h**, The spatial offset between excitatory and inhibitory presynaptic ensembles ($n=16$) predicts the direction selectivity index (DSI) measured from the postsynaptic neuron responses. Linear fit (red) with 95% confidence interval (grey). ** $r=0.65, P=7 \times 10^{-3}, F$ -test. Circles represent experiments from *CaMK2a-GCaMP6* mice; squares indicate experiments from *GAD2-NLS-mCherry* mice.

neuron (Fig. 3c–h). Excitatory presynaptic neurons were densest in locations that extended along the preferred orientation of the postsynaptic neuron³, and favoured the side opposite to the neuron's preferred direction (Fig. 3b, c). By contrast, inhibitory presynaptic neurons were arranged more proximally and favoured the side ahead of the neuron's preferred direction (Fig. 3b, d). To pool results across postsynaptic neurons, we rotated the presynaptic densities so that the resulting preferred direction of the postsynaptic neuron pointed rightwards (Fig. 3e, f). The combined excitatory presynaptic ensemble was elongated along the preferred orientation of the postsynaptic neuron (that is, vertically), and displaced opposite to the preferred direction of the neuron (that is, to the left) (Fig. 3g). By contrast, the combined inhibitory presynaptic ensemble was local, concentric and displaced ahead of the preferred direction of the postsynaptic neuron (that is, to the right) (Fig. 3h). These spatial patterns were present both in inputs from L2/3 and in inputs from L4 (Extended Data Fig. 10g–l). They manifested only in precise relation to the visual preferences and local retinotopy of each postsynaptic neuron: ignoring these factors when averaging across ensembles would yield an apparent concentric arrangement of inhibition and excitation (Extended Data Fig. 10a–f).

To quantify these differences between excitatory and inhibitory ensembles, we calculated the angular density in the visual space of excitatory and inhibitory presynaptic neurons relative to the postsynaptic neuron (Fig. 3i, j). The excitatory ensemble favoured visual sectors that are orthogonal to the preferred direction—that is, parallel to the preferred orientation, with a deeper trough ahead of the preferred direction (shown in red in Fig. 3j). The inhibitory ensemble was more equally distributed around the postsynaptic neuron, with a trough opposite to the postsynaptic preferred direction (shown in blue in Fig. 3j).

The preferred orientation of postsynaptic neurons accorded with the spatial elongation of excitatory, but not inhibitory, presynaptic ensembles (Fig. 3k, l). The angle of elongation of the presynaptic excitatory ensemble correlated significantly with the preferred orientation of the postsynaptic neuron ($r=0.72, P_r=7 \times 10^{-3}, P_V=10^{-4}$) (Fig. 3k). This correlation did not result from anisotropies of the retinotopic map: the correlation was significantly higher than in surrogate ensembles crafted to be isotropic in the cortex with similar distances from the postsynaptic neurons, which favoured horizontal elongation ($P_{r,\text{rand}}=10^{-3}, P_{V,\text{rand}}<10^{-4}$) (Fig. 3k). Inhibitory presynaptic ensembles did not significantly align with the preferred orientation of the postsynaptic neuron ($r=-0.07, P_r=0.77, P_V=0.12$) (Fig. 3l). This contrast between elongated excitation and concentric inhibition would enhance responses to the preferred orientation.

Presynaptic connectivity also matched the preferred direction of the postsynaptic neuron, with a consistent spatial offset between excitation and inhibition (Fig. 3m, n). Excitatory presynaptic neurons were significantly more abundant opposite to the preferred direction of the postsynaptic neuron than ahead of it ($P_W=0.035, n=16$) (Fig. 3n). Inhibitory presynaptic neurons showed the reverse effect ($P_W=3 \times 10^{-3}$) (Fig. 3o). Therefore, the balance between excitatory and inhibitory inputs invariably favoured visual sectors opposite to the preferred direction of the postsynaptic neuron ($P_W=4 \times 10^{-4}$) (Fig. 3m).

Intracortical origin of direction tuning

The spatial offset between excitation and inhibition provides a candidate circuit for direction selectivity (Fig. 4a–f). Intracellular recordings^{38,39} from L2/3 V1 neurons have demonstrated that visual stimulation triggers excitatory and inhibitory conductances staggered by 10 ms (Fig. 4b). Excitation and inhibition thus are offset not only in space, but also in time. This arrangement can provide direction selectivity^{13–17,28,40}: a stimulus approaching the postsynaptic neuron in the preferred direction would recruit first excitation, and then inhibition (Fig. 4c)—evoking a large response (Fig. 4d). Conversely, movement in the opposite direction would first recruit inhibition, resulting in a delay that would suppress the subsequent excitation (Fig. 4e, f).

This model makes a testable prediction: neurons with excitatory and inhibitory inputs that are more spatially offset should show stronger direction selectivity (Fig. 4g, h). In support of this prediction, the three neurons with the weakest direction selectivity had excitatory and inhibitory presynaptic ensembles that largely overlapped (Fig. 4g). Conversely, in the three neurons with the strongest direction selectivity, the excitatory and inhibitory presynaptic ensembles were strongly offset (Fig. 4g). To verify the prediction of the model, we estimated the net input (excitation minus inhibition) received by each postsynaptic neuron in sectors opposite or ahead of its preferred direction (Fig. 3m). We then computed a predicted direction selectivity index by subtracting the normalized net input in the two sectors. This direction selectivity index was predicted purely from the spatial pattern of presynaptic ensembles, but strongly correlated with the direction selectivity index of the postsynaptic neurons that was measured from visual responses ($r=0.65, P=7 \times 10^{-3}$) (Fig. 4h). Therefore, the spatial offset of excitatory and inhibitory presynaptic ensembles predicts not only the preferred direction of a neuron (Fig. 3m), but also the strength of its direction selectivity (Fig. 4h).

Discussion

We have revealed a precise spatial patterning of excitatory and inhibitory connections to L2/3 neurons, which can strengthen orientation tuning and establish direction selectivity without connections from co-tuned neurons. The standard model for selectivity in L2/3 relies on excitatory co-tuning^{2–6,8,41,42}. However, we have shown that the direction preference of a L2/3 neuron does not correlate with that of its

presynaptic excitatory cells. Instead, it strongly correlates with the spatial pattern and offset of excitatory and inhibitory inputs. Given the delay between excitation and inhibition^{38,39}, this offset may explain direction selectivity^{13–17,28,40} in L2/3.

Our results open several questions, including whether spatial connectivity arises during development, is shaped by visual experience, is different across inhibitory neuron types and relies on similar mechanisms across species. Rabies tracing may help to address these questions, especially if it were confirmed to travel only across synapses and to sample evenly among synaptic inputs¹². It would also be important to measure synaptic weights, which may have an important role in selectivity^{4,6,22}.

Direction selectivity is computed at multiple stages along the visual pathway. It emerges in the retina through asymmetric excitation and inhibition^{13–17}, and is relayed to cortical L1 via a dedicated thalamic pathway^{43,44}. Direction selectivity is then computed anew⁴⁵ in cortical L4, through integration of spatiotemporally displaced thalamic inputs^{40,45}. Our findings suggest that, in mice, it is computed yet again in L2/3. Moreover, in primates it may be computed at yet another stage, in the middle temporal visual area⁴⁶ (area MT).

Our results raise the question of why direction selectivity would be computed so many stages. Perhaps, at each stage it is useful to detect spatiotemporal gradients in the activity of the previous stage. The mechanisms that compute these spatiotemporal gradients appear to be conserved across stages. For example, the spatially offset arrangement of excitation and inhibition in L2/3 resembles the circuit for direction-selective ganglion cells in the retina^{13–17}. The cortex thus replicates circuit motifs seen in the retina, and the reappearance of these motifs suggests they might be canonical across brain regions.

Online content

Any methods, additional references, Nature Research reporting summaries, source data, extended data, supplementary information, acknowledgements, peer review information; details of author contributions and competing interests; and statements of data and code availability are available at <https://doi.org/10.1038/s41586-020-2894-4>.

- Wertz, A. et al. Single-cell-initiated monosynaptic tracing reveals layer-specific cortical network modules. *Science* **349**, 70–74 (2015).
- Ko, H. et al. Functional specificity of local synaptic connections in neocortical networks. *Nature* **473**, 87–91 (2011).
- Iacaruso, M. F., Gasler, I. T. & Hofer, S. B. Synaptic organization of visual space in primary visual cortex. *Nature* **547**, 449–452 (2017).
- Lee, W. C. et al. Anatomy and function of an excitatory network in the visual cortex. *Nature* **532**, 370–374 (2016).
- Wilson, D. E., Whitney, D. E., Scholl, B. & Fitzpatrick, D. Orientation selectivity and the functional clustering of synaptic inputs in primary visual cortex. *Nat. Neurosci.* **19**, 1003–1009 (2016).
- Cossell, L. et al. Functional organization of excitatory synaptic strength in primary visual cortex. *Nature* **518**, 399–403 (2015).
- Wilson, D. E., Scholl, B. & Fitzpatrick, D. Differential tuning of excitation and inhibition shapes direction selectivity in ferret visual cortex. *Nature* **560**, 97–101 (2018).
- Chen, T. W. et al. Ultrasensitive fluorescent proteins for imaging neuronal activity. *Nature* **499**, 295–300 (2013).
- Jia, H., Rochefort, N. L., Chen, X. & Konnerth, A. Dendritic organization of sensory input to cortical neurons in vivo. *Nature* **464**, 1307–1312 (2010).
- Packer, A. M. & Yuste, R. Dense, unspecific connectivity of neocortical parvalbumin-positive interneurons: a canonical microcircuit for inhibition? *J. Neurosci.* **31**, 13260–13271 (2011).
- Hofer, S. B. et al. Differential connectivity and response dynamics of excitatory and inhibitory neurons in visual cortex. *Nat. Neurosci.* **14**, 1045–1052 (2011).
- Wickersham, I. R. et al. Monosynaptic restriction of transsynaptic tracing from single, genetically targeted neurons. *Neuron* **53**, 639–647 (2007).
- Barlow, H. B. & Levick, W. R. The mechanism of directionally selective units in rabbit's retina. *J. Physiol. (Lond.)* **178**, 477–504 (1965).
- Fried, S. I., Münch, T. A. & Werblin, F. S. Mechanisms and circuitry underlying directional selectivity in the retina. *Nature* **420**, 411–414 (2002).
- Briggman, K. L., Helmstaedter, M. & Denk, W. Wiring specificity in the direction-selectivity circuit of the retina. *Nature* **471**, 183–188 (2011).
- Vaney, D. I., Sivyer, B. & Taylor, W. R. Direction selectivity in the retina: symmetry and asymmetry in structure and function. *Nat. Rev. Neurosci.* **13**, 194–208 (2012).
- Kim, J. S. et al. Space-time wiring specificity supports direction selectivity in the retina. *Nature* **509**, 331–336 (2014).
- Alonso, J. M. & Martinez, L. M. Functional connectivity between simple cells and complex cells in cat striate cortex. *Nat. Neurosci.* **1**, 395–403 (1998).
- Priebe, N. J. Mechanisms of orientation selectivity in the primary visual cortex. *Annu. Rev. Vis. Sci.* **2**, 85–107 (2016).
- Isaacson, J. S. & Scanziani, M. How inhibition shapes cortical activity. *Neuron* **72**, 231–243 (2011).
- Liu, B. H. et al. Broad inhibition sharpens orientation selectivity by expanding input dynamic range in mouse simple cells. *Neuron* **71**, 542–554 (2011).
- Znamenskiy, P. et al. Functional selectivity and specific connectivity of inhibitory neurons in primary visual cortex. Preprint at <https://doi.org/10.1101/294835> (2018).
- Lee, S. H. et al. Activation of specific interneurons improves V1 feature selectivity and visual perception. *Nature* **488**, 379–383 (2012).
- Atallah, B. V., Bruns, W., Carandini, M. & Scanziani, M. Parvalbumin-expressing interneurons linearly transform cortical responses to visual stimuli. *Neuron* **73**, 159–170 (2012).
- Wilson, N. R., Runyan, C. A., Wang, F. L. & Sur, M. Division and subtraction by distinct cortical inhibitory networks *in vivo*. *Nature* **488**, 343–348 (2012).
- Ma, W. P. et al. Visual representations by cortical somatostatin inhibitory neurons—selective but with weak and delayed responses. *J. Neurosci.* **30**, 14371–14379 (2010).
- Monier, C., Chavane, F., Baudot, P., Graham, L. J. & Frégnac, Y. Orientation and direction selectivity of synaptic inputs in visual cortical neurons: a diversity of combinations produces spike tuning. *Neuron* **37**, 663–680 (2003).
- Livingstone, M. S. Mechanisms of direction selectivity in macaque V1. *Neuron* **20**, 509–526 (1998).
- Xu, X. et al. Primary visual cortex shows laminar-specific and balanced circuit organization of excitatory and inhibitory synaptic connectivity. *J. Physiol. (Lond.)* **594**, 1891–1910 (2016).
- Adesnik, H. & Scanziani, M. Lateral competition for cortical space by layer-specific horizontal circuits. *Nature* **464**, 1155–1160 (2010).
- Holmgren, C., Harkany, T., Svänenfors, B. & Zilberman, Y. Pyramidal cell communication within local networks in layer 2/3 of rat neocortex. *J. Physiol. (Lond.)* **551**, 139–153 (2003).
- Weiler, S. et al. Relationship between input connectivity, morphology and orientation tuning of layer 2/3 pyramidal cells in mouse visual cortex. Preprint at [bioRxiv https://doi.org/10.1101/2020.06.03.127191](https://doi.org/10.1101/2020.06.03.127191) (2020).
- Sun, W., Tan, Z., Mensh, B. D. & Ji, N. Thalamus provides layer 4 of primary visual cortex with orientation- and direction-tuned inputs. *Nat. Neurosci.* **19**, 308–315 (2016).
- Ringach, D. L. et al. Spatial clustering of tuning in mouse primary visual cortex. *Nat. Commun.* **7**, 12270 (2016).
- Marques, T., Nguyen, J., Fioreze, G. & Petreanu, L. The functional organization of cortical feedback inputs to primary visual cortex. *Nat. Neurosci.* **21**, 757–764 (2018).
- Bonin, V., Histed, M. H., Yurgenson, S. & Reid, R. C. Local diversity and fine-scale organization of receptive fields in mouse visual cortex. *J. Neurosci.* **31**, 18506–18521 (2011).
- Garrett, M. E., Nauhaus, I., Marshel, J. H. & Callaway, E. M. Topography and areal organization of mouse visual cortex. *J. Neurosci.* **34**, 12587–12600 (2014).
- Haider, B., Häusser, M. & Carandini, M. Inhibition dominates sensory responses in the awake cortex. *Nature* **493**, 97–100 (2013).
- Liu, B. H. et al. Intervening inhibition underlies simple-cell receptive field structure in visual cortex. *Nat. Neurosci.* **13**, 89–96 (2010).
- Li, Y. T., Liu, B. H., Chou, X. L., Zhang, L. I. & Tao, H. W. Strengthening of direction selectivity by broadly tuned and spatiotemporally slightly offset inhibition in mouse visual cortex. *Cereb. Cortex* **25**, 2466–2477 (2015).
- Lien, A. D. & Scanziani, M. Tuned thalamic excitation is amplified by visual cortical circuits. *Nat. Neurosci.* **16**, 1315–1323 (2013).
- Li, Y. T., Ibrahim, L. A., Liu, B. H., Zhang, L. I. & Tao, H. W. Linear transformation of thalamocortical input by intracortical excitation. *Nat. Neurosci.* **16**, 1324–1330 (2013).
- Hillier, D. et al. Causal evidence for retina-dependent and -independent visual motion computations in mouse cortex. *Nat. Neurosci.* **20**, 960–968 (2017).
- Cruz-Martin, A. et al. A dedicated circuit links direction-selective retinal ganglion cells to the primary visual cortex. *Nature* **507**, 358–361 (2014).
- Lien, A. D. & Scanziani, M. Cortical direction selectivity emerges at convergence of thalamic synapses. *Nature* **558**, 80–86 (2018).
- Thiele, A., Distler, C., Korbacher, H. & Hoffmann, K. P. Contribution of inhibitory mechanisms to direction selectivity and response normalization in macaque middle temporal area. *Proc. Natl. Acad. Sci. USA* **101**, 9810–9815 (2004).

Publisher's note Springer Nature remains neutral with regard to jurisdictional claims in published maps and institutional affiliations.

Methods

All experimental procedures were conducted in accordance with the UK Animals Scientific Procedures Act (1986). Experiments were performed at University College London under personal and project licences released by the Home Office following appropriate ethics review. No statistical methods were used to predetermine sample size. The experiments were not randomized and investigators were not blinded to allocation during experiments and outcome assessment.

Breeding of transgenic mice

Experiments were performed on twenty 7–12-week-old mice of both sexes, maintained on a 12-h light/dark cycle, at 20–24 °C and 45–65% humidity, in individually ventilated cages. Sixteen experiments involved mice expressing GCaMP6 in CaMK2a-positive neurons (referred to as *CaMK2a-GCaMP6*) through different transgenic strategies. Five mice were *CaMK2a-tTA;Emx1-cre;TIGRE-Ins-TRE-LSL-GCaMP6f* (*TIGRE* is also known as *Igs7*) (Ai93D) triple-transgenic mice⁴⁷, expressing the calcium indicator GCaMP6f in all cortical excitatory neurons. Six mice were *CaMK2a-tTA;Emx1-cre;Tigre-Ins-TRE-LSL-GCaMP6s* (Ai94D) triple-transgenic mice⁴⁷, expressing the calcium indicator GcaMP6s in all cortical excitatory neurons. Five mice were *CaMK2a-tTA;tetO-GCaMP6s* double-transgenic mice⁴⁸, expressing GCaMP6s in all cortical excitatory neurons. These transgenic mice were bred from the following parental lines: *Emx1-IRES-cre* (stock no. 005628, The Jackson Laboratory⁴⁹); *CaMK2a-tTA* (stock no. 007004⁵⁰); Ai93D (stock no. 024103⁴⁷); Ai94D (stock no. 024104⁴⁷); *TRE-GCaMP6s* (stock no. 024742⁴⁸). Differences in the GCaMP6 variants used did not affect the results of the study, because data in each experiment were compared against internal controls. A subset of four experiments involved instead *GAD2-T2A-NLS-mCherry* mice, which express the far-red fluorescent protein mCherry localized to the nucleus of inhibitory neurons (stock no. 023140⁵¹).

Surgical procedures

Mice were anaesthetized with isoflurane (1–2% in oxygen), their body temperature was monitored and kept at 37–38 °C using a closed-loop heating pad, and the eyes were protected with ophthalmic gel (Viscotears Liquid Gel, Alcon). An analgesic (Rimadyl, 5 mg/kg) was administered subcutaneously before the procedure, and orally on subsequent days. Whenever the procedure exposed the brain, dexamethasone (0.5 mg/kg, IM) was administered intramuscularly 30 min before the procedure to prevent brain oedema. The exposed brain was constantly perfused with artificial cerebrospinal fluid (150 mM NaCl, 2.5 mM KCl, 10 mM HEPES, 2 mM CaCl₂, 1 mM MgCl₂; pH 7.3 adjusted with NaOH, 300 mOsm).

The first surgery involved the implant of a head-plate over the right hemisphere of the cranium. The head was shaved and disinfected; the cranium was exposed and covered with biocompatible cyanoacrylate glue (Vetbond, 3M). A stainless-steel head plate with a 10-mm circular opening was secured over the skull using dental cement (Super-Bond C&B, 10 Sun Medical). The exposed bone inside the chamber was covered by a thin layer of dental cement and sealed off with silicone elastomer (Kwik-Cast, WPI).

The second surgery was necessary for targeted neuron electroporation. A 1.5–2-mm-wide square craniotomy was opened over V1 (centred at –3.3 mm anterior–posterior, 2.8 mm medial–lateral from bregma). Following the electroporation, the craniotomy was sealed with a glass cranial window, assembled from a circular cover glass (3-mm diameter, 100-μm thickness) glued to a smaller custom-made glass square insert (1.5–2-mm wide, 300-μm thickness) with index-matched UV curing adhesive (Norland no. 61).

We performed a third surgery to inject a rabies virus (RV) for single-neuron-initiated monosynaptic tracing^{52–55}. The cranial window and the dura mater were removed⁵⁶; 100–200 nl of *EnvA-dG-dsRedExpress-RV* (10⁸–10⁹ plaque-forming units per ml) were

injected through a 20–30-μm borosilicate capillary connected to a pneumatic injector (Nanoject, Drummond Scientific). The injection was targeted about 100–200 μm from the electroporated neuron. Afterwards, a permanent glass window was implanted.

In experiments involving *GAD2-T2A-NLS-mCherry* mice (Extended Data Fig. 6), GCaMP6s was delivered pan-neuronally with an adenoviral vector at about postnatal day 28. The scalp was shaved and incised to expose the skull over V1. Three approximately 250-μm-wide craniotomies—spaced as an approximately 1-mm equilateral triangle—were targeted to the central part of V1. Two hundred nanolitres of *AAV2.1-Syn-GCaMP6s* (about 10¹¹ genome copies (GC) per ml) were injected through each craniotomy, distributing the volume between L5 and L2/3. Finally, the craniotomies were covered with mineral oil and the skin sutured over the exposed scalp.

In two control experiments (Extended Data Fig. 4g), the red fluorescent protein tdTomato was sparsely expressed by injecting diluted *AAV2.1-CaMK2a-cre* (about 10⁷ GC per ml) and concentrated *AAV2.1-Syn-flex-tdTomato* (about 10¹² GC per ml).

Histology

Two weeks after the rabies virus injection, mice were anaesthetized with isoflurane, injected with sodium pentobarbital (0.01 ml/g) and perfused transcardially with ice-cold phosphate buffered saline (PBS), followed by 4% ice-cold PFA in PBS. The brain was extracted, postfixed for 24 h in 4% PFA PBS at 4 °C, and finally transferred to a 30% sucrose PBS at 4 °C. Fifty-micrometre-thick coronal sections were serially cut on a vibratome to span the whole V1, washed in PBS, blocked with a 0.3% Triton-X100, 1% BSA solution in PBS and processed with the following antibodies: mouse anti-GAD67 primary antibody (1:1,500, Millipore MAB5406), donkey anti-mouse IgG Alexa Fluor 647 conjugate secondary antibody (1:800, Merk Millipore AP192SA6). Sections were mounted on SuperFrost slides (Molecular Probes), air dried and coverslipped with Fluoromount (Sigma-Aldrich). Z-stack tile scans of each slide were imaged with a Nikon Eclipse Ti2-E inverted epifluorescence microscope and manually aligned to the corresponding sections from *in vivo* z-stacks. Images were high-pass-filtered for display (Extended Data Fig. 5).

Targeted single-cell electroporation with survival control

Targeted single-cell electroporation^{57,58} was performed under a Sutter-MOM two-photon microscope, equipped with a low magnification (16×) high NA (0.8) water immersion objective lens (Nikon), an epifluorescence imaging module and a femtosecond pulsed laser (Chameleon Ultra II, Coherent) tuned at 820 nm. The microscope was controlled using ScanImage v.3.8⁵⁹.

Borosilicate patch pipettes (resistance 10–14 MΩ) were crafted with a vertical puller (Narishige) and filled with intracellular solution (133 mM KMeSO₄, 7 mM KCl, 10 mM HEPES, 2 mM Mg-ATP, 2 mM Na₂-ATP, 0.5 mM Na₂-GTP, 0.05 mM EGTA; pH 7.2, adjusted with KOH, 280–290 mOsm; filtered using a 0.45-mm syringe filter). The intracellular solution also contained 50 μM of the red fluorescent dye Alexa Fluor 594 and 3 plasmids with the following concentrations⁵⁴: 100 μg/μl *pCAG-dsRed2* (Addgene no. 15777), 200 μg/μl *pCMV-oG* (Addgene 74288⁶⁰; or *pCMV-G* in a subset of experiments, Addgene 15785) and 100 μg/μl *pCAG-TVA800* (Addgene 15788).

The pipette was manoeuvred with a micromanipulator (Junior 4 axis, Luigs & Neumann) and pushed through the dura, while applying positive pressure (about 150 mBar) and monitoring the pipette resistance with an electroporator for *in vivo* transfections (Axoprotector 800A, Molecular Devices). The pressure was then reduced to 30–50 mBar: the diffusion of the red dye in the extracellular space counterstained neuronal somas, while GCaMP6 allowed targeting of excitatory cells (Fig. 1b). The pipette tip was pushed onto a neuronal soma, and, upon an approximately 30% increase in resistance, neurons were electroporated with a single pulse train at –11 V, 100 Hz, 0.5-ms pulse width, 1-s duration, and the pipette was swiftly retracted.

Article

Three criteria were used as signature of successful electroporation and recovery of a neuron from the electroporation shock (Extended Data Fig. 1): immediate filling of the soma with Alexa Fluor 594 (Extended Data Fig. 1e, g); retraction of the pipette without pulling of the neuronal membrane (Extended Data Fig. 1e); and sustained somatic GCaMP6 fluorescence at 820 nm relative to the surrounding neuropil (Extended Data Fig. 1h–l). Electroporated neurons were monitored for 3–10 min after electroporation. With these criteria, we could predict which electroporation attempts were successful with an 80% success rate.

We performed up to 5 electroporation attempts per mouse, at sites spaced >500 μm apart. Transgene expression of electroporated cells was assessed 1–3 days after electroporation (Extended Data Fig. 1f, i, k).

Targeted photo-ablation of supernumerary electroporated neurons

We selected a single target for monosynaptic tracing by photo-ablating any supernumerary electroporated neurons (Extended Data Fig. 2). The galvanometric mirrors were centred on the soma of the target neuron, and pulses of high-intensity 820-nm two-photon illumination (>100 mW) were delivered for 10–20 s. Neurons were imaged during and between the pulses to titrate the extent of the photodamage and avoid damage to the surrounding neurons. The outcome of the photo-ablation was ascertained the following day via functional imaging.

Two-photon imaging of neuronal responses

Recordings of neuronal activity were performed with a standard resonant-scanning two-photon microscope (B-Scope, Thorlabs), equipped with a Nikon 16 \times , 0.8 NA objective mounted on a piezoelectric z-drive (PIFOCP-725.4CA, Physik Instrumente, range 400 μm) for volumetric multi-plane imaging. The microscope was controlled using ScanImage v.4.2⁵⁹. Excitation light was provided by a femtosecond laser (Chameleon Ultra II, Coherent), tuned between 780 and 1,020 nm. Laser power was depth-adjusted between 30 and 300 mW, and synchronized with piezo position using an electro-optical modulator (M350-80LA, Conoptics). Sample fluorescence was collected in a green (525/50 nm) and a red (605/70 nm) channel.

Fields of view (FOVs), centred on the postsynaptic neuron position, were imaged with a resolution of 512 \times 512 pixels at 30 Hz. FOVs typically spanned 150–200 μm for the initial imaging of the postsynaptic neuron, and between 500 and 850 μm for the imaging of presynaptic ensembles. For volumetric imaging of GCaMP6s, the objective was scanned across 10 planes, separated by 15–20 μm in depth, resulting in an effective sampling rate of 3 Hz. For volumetric imaging of GCaMP6f, only 5 planes were used instead, with an effective sampling rate of 6 Hz. A full cortical column was tiled by serially repeating volumetric acquisitions from the cortical surface to L5. To acquire structural z-stacks, the piezoelectric z-drive moved the objective in steps of 1 μm .

Imaging sessions lasted 2–4 h and included 2–3 h of effective imaging time. During the imaging sessions, mice were head-fixed on an airflow-suspended spherical treadmill. Recordings started on the day after electroporation and lasted up to two weeks after rabies virus injection (Extended Data Fig. 3).

Spectral unmixing

We devised a method to spectrally separate dsRed and mCherry fluorescence (Extended Data Fig. 6), the overlapping emission spectra⁶¹ (www.fpbbase.org) of which could not be differentiated using the acquisition channels of our two-photon microscope (Extended Data Fig. 6a). For each FOV, we acquired images at four excitation wavelengths (λ): 780, 890, 970 and 1,020 nm. The two shortest wavelengths were chosen to obtain strong signals from either mCherry or dsRed while maximizing the ratio between their action cross-sections^{61,62} (Extended Data Fig. 6b, c). The 1,020-nm wavelength was used to compensate for the

degrading efficacy of 780 nm imaging with cortical depth. Finally, the 970-nm wavelength was used for functional imaging. The objective position was adjusted to compensate for focal changes at each excitation wavelength. The G channel (\mathbf{G}_λ) provided a direct readout of the GCaMP6 signal, with negligible bleed-through from the sparse dsRed and mCherry fluorescence (Extended Data Fig. 6d). The R channel (\mathbf{R}_λ) instead reflected a linear mixture of GCaMP6s, dsRed and mCherry fluorescence (Extended Data Fig. 6e). Because the GCaMP6 labelling was dense—and both mCherry and dsRed labelling were sparse—contributing to a minority of pixels, we could compute the GCaMP6 signal contributing to \mathbf{R}_λ by piecewise robust linear regression of \mathbf{R}_λ against \mathbf{G}_λ (Extended Data Fig. 6f). We binned the pixels from \mathbf{G}_λ in 50 intervals (i), and took the median of each interval to represent the component of \mathbf{R}_λ explained by GCaMP6 fluorescence. We then computed the image \mathbf{M}_λ corresponding to the linear mixture of mCherry and dsRed signals (Extended Data Fig. 6g) as $\mathbf{M}_\lambda = \mathbf{R}_\lambda - \alpha_{\lambda i} \mathbf{G}_{\lambda i} - \beta_{\lambda i}$, in which the parameters $\alpha_{\lambda i}$ and $\beta_{\lambda i}$ are the result of the robust linear regression. Finally, we decomposed \mathbf{M}_λ in the $\mathbf{R}_{\text{mCherry}}$ and $\mathbf{R}_{\text{dsRed}}$ source images (Extended Data Fig. 6h–j). The linear problem was formulated as:

$$\mathbf{M}_\lambda = [\rho \quad \kappa]_\lambda \times \begin{bmatrix} \mathbf{R}_{\text{dsRed}} \\ \mathbf{R}_{\text{mCherry}} \end{bmatrix},$$

in which ρ_λ and κ_λ are the linear mixture coefficients of the two fluorophores. These coefficients should theoretically correspond to the product between the action cross section at wavelength λ and the integral of the emission spectrum captured by the red channel of the microscope. However, we could neither provide constant excitation intensity at each wavelength nor control for the contribution of scattering and autofluorescence at different imaging depths. To compensate for these issues, we used an iterative custom linear unmixing algorithm to learn both the source images and new mixing coefficients, constructed to return maximally uncorrelated source images while minimizing the quadratic reconstruction error over the data. Starting from the theoretical mixing coefficients, we iterated between estimating the source images while keeping the mixing coefficient fixed and optimizing the mixing coefficients while keeping the source images fixed, until convergence.

Visual stimulation

Visual stimuli were generated in MATLAB (MathWorks) using the Psychophysics Toolbox⁶³ (www.psychtoolbox.org) and displayed on 3 gamma-corrected LCD monitors (Iiyama ProLite E1980SD, refresh rate 60 Hz, connected through a Matrox TripleHead2Go Digital Edition multi-display adaptor) surrounding the mouse at 90° to each other. The LCD screens were covered with Fresnel lenses to correct for viewing angle inhomogeneity of the LCD luminance⁶⁴. The mouse was positioned at the centre of the U-shaped monitor arrangement at 20 cm from all 3 monitors, so that the monitors spanned ±135° of horizontal and ±35° of the vertical visual field.

Sparse, spatial white noise stimuli were used to map the retinotopy of the imaged area and estimate the receptive field of neurons. Patterns of sparse black and white squares (4.5–6° of visual field) on a grey background were presented at 5 Hz, typically in 10-min sequences repeated 3 times for each FOV. At any point in time, each square had a 2–5% probability of being non-grey, independent of the other squares.

To measure direction and orientation tuning, we presented gratings drifting in 12 directions, centred on the receptive field of the postsynaptic neuron. Gratings were presented in a circular window of 30–80°, depending on the size of the imaged FOV, at 100% contrast on a grey uniform background, with a spatial frequency of 0.05 cycles per degree, and a temporal frequency of 2 Hz. In some experiments, to stimulate more neurons, we also varied the spatial and temporal frequency of the gratings between 0.05–0.5 cycles per degree and 0.5–5 Hz. Six to ten repeats of each stimulus were presented for each FOV. Stimuli lasted 1–2 s, separated by 3–4 s of grey background.

Processing of two-photon data

Two-photon data were pre-processed using Suite2p⁶⁵. The pipeline included image registration, segmentation of active region of interest (ROIs) and estimation of the neuropil signal contaminating each ROI. The final selection of ROIs was curated manually to include only neuronal somas and discard spurious or noisy ROIs. Active presynaptic neurons expressing dsRed were identified by inspecting the average dsRed image for each acquisition. Simultaneously recorded neuronal responses from each imaged volume were aligned to a common time reference by interpolation.

The neuropil signal was weighted by a correction factor α , determined separately for each ROI⁶⁶, before being subtracted. The correction factor was estimated from the linear relationship between the lowest somatic fluorescence compatible with any value of fluorescence in the neuropil. For each neuron i , the neuropil signal $N_i(t)$ was binned into 20 intervals; for each interval, the fifth percentile of the matching time-points of raw somatic fluorescence $F_i(t)$ was measured as an estimate of baseline fluorescence. α_i was then computed by linear regression between the median of each neuropil interval and estimates of baseline fluorescence, to accurately fit the lower envelope of the scatterplot of neuropil versus somatic fluorescence. The corrected fluorescence was computed as $F_i(t) - \alpha_i N_i(t)$. Finally, fluorescence time courses were z-scored for further analysis.

Volumetric imaging often resulted in the same neurons being imaged multiple times in different imaging planes: duplicates of the same neuron were identified as ROIs with a centre of mass that was closer than 5 μm in lateral distance and closer than 20 μm in depth and had a signal higher than 0.5.

For longitudinal imaging experiments of presynaptic neurons before and after rabies tracing (Extended Data Fig. 3e–h), ROIs corresponding to putative presynaptic neurons were manually identified by comparing the outputs of Suite2P before and after tracing. Subsequently, templates corresponding to the same neuron across recordings were matched on the basis of image correlation and relative 3D position. Matches were further curated manually to eliminate false positives.

Quantification of the rabies tracing and associated neuronal mortality

The progression of rabies tracing over days was monitored using structural and functional z-stacks. The viability of the postsynaptic neuron (p_d) was evaluated on the basis of progressive signs of apoptosis: elevated intracellular calcium, lack of functional responses and dendritic blebbing (Extended Data Fig. 3a). The number of presynaptic neurons observed each day (O_d) was manually counted from each z-stack (Extended Data Fig. 3b). Missing observations were interpolated assuming a sigmoidal progression of the tracing. Because of the cytotoxicity of the rabies virus, O_d values may not correspond to the total number of presynaptic neurons traced (T_d): some presynaptic neurons could progressively become sick and disappear with the passing of days (Extended Data Fig. 3c). If N_d is the number of new presynaptic neurons traced by the rabies virus on day d , the total number of traced neurons can be calculated as

$$T_d = \sum_{i=1}^d N_i,$$

and the population mortality (M_d) curve of presynaptic neurons as $M_d = (T_d - O_d)/(T_d)$.

Although we could not directly measure N_d , we could estimate it from O_d by assuming the viability of each presynaptic neuron, once infected by the rabies virus, would degrade at the same rate p_d measured for the postsynaptic neurons (Extended Data Fig. 3c). This assumption yields a worst-case scenario estimate of population mortality for presynaptic

neurons, which—being transduced by fewer virions than the postsynaptic neuron—should survive longer. At the beginning of the experiment, $N_1 = O_1 = 0$, as the tracing has not begun yet. We then iteratively estimated the number of neurons appearing each new day of tracing as:

$$N_d = O_d - \sum_{i=1}^{d-1} N_i \times p_{d-i},$$

which describes the number of neurons observed at day d minus the number of neurons that survived from previous days (Extended Data Fig. 3c).

Classification of excitatory and inhibitory neurons

For experiments in *CaMK2a–GCaMP6* transgenic mice, a custom algorithm was used to identify and classify presynaptic neurons either as excitatory or inhibitory (Extended Data Fig. 4). Serial volumetric-imaging time series were averaged to obtain high signal-to-noise ratio z-stacks, with a green GCaMP6 channel (highlighting GCaMP6-expressing neurons) and a red dsRed channel (highlighting presynaptic neurons). An iterative thresholding algorithm was used to segment somatic masks of presynaptic neurons from the red channel; somatic masks were inspected and curated manually, and spurious or out-of-focus neurons were discarded (Extended Data Fig. 4a, b). Then, the phase correlation (that is, whitened cross-correlation) between the somatic mask of each neuron and its GCaMP6 fluorescence image was used to classify neurons as GCaMP6-positive or GCaMP6-negative cells (Extended Data Fig. 4a–d). The amplitude of the central correlation peak and the s.d. of the correlation values inside a 5- μm annulus around the peak were used to fit a bilinear classification boundary separating putative excitatory GCaMP6-expressing neurons from putative inhibitory GCaMP6-negative neurons (Extended Data Fig. 4c). This classification was computed independently for each experiment. The sensitivity and specificity of the algorithm (about 90–95%) were tested in control experiments in which a red protein was sparsely expressed only in excitatory neurons (Extended Data Fig. 4e) and by immunohistochemistry (Extended Data Fig. 5).

For experiments in *GAD2–T2A–NLS–mCherry* transgenic mice, putative excitatory and putative inhibitory neurons were sorted on the basis of the expression of nuclear mCherry.

The cortical position of presynaptic neurons was used to estimate their radial and layer densities around the postsynaptic neuron. Cortical probability densities were calculated in 625- μm^2 bins (x) and smoothed with a 25- μm -wide Gaussian kernel. Probability densities (P_x) were calculated independently for excitatory and inhibitory presynaptic ensembles, by dividing the number of neurons in each spatial bin (N_x) by the total number of traced neurons, using:

$$P_x = \frac{N_x}{\sum_x N_x}.$$

Analysis of neuronal responses

All neurons identified by Suite2P were considered responsive and included for further analysis. Stimulus-triggered responses were computed as the difference between the z-scored fluorescent trace and the 20th percentile of the baseline activity 1 s before stimulus presentation. Stimulus-triggered average responses and s.e.m. were obtained across responses to the same type of stimuli.

Responses to drifting gratings were quantified as the integral of the fluorescent response in a 3-s window following the onset of stimulation. The preferred orientation and direction of motion were defined according to the grating that elicited the maximal response. For postsynaptic neurons only, the preferred direction and orientation were computed by fitting a double-Gaussian tuning curve to the data.

Article

The direction selectivity index of postsynaptic neurons was computed as

$$DSI = \frac{(R_{\text{pref}} - R_{\text{anti}})}{(R_{\text{pref}} + R_{\text{anti}})},$$

in which R_{pref} is the response to the preferred direction, and R_{anti} is the response to the direction opposite to the preferred (anti-preferred). Neuronal responsiveness was quantified as the average response to the preferred stimulus, z-scored with respect to the s.d. of the blank trials. To compare across sessions, responsiveness was normalized to the median responsiveness across all simultaneously recorded neurons.

Wide-field receptive field centres were estimated from population retinotopic maps (Extended Data Fig. 9a–c). For this analysis, imaging time series were denoised and compressed by singular value decomposition. Recordings from different planes were z-scored and concatenated to produce a single movie for each imaging volume. Wide-field receptive fields were calculated by reverse correlation between fluorescence signals and the absolute changes in luminance of the stimulus. First, a global receptive field was fit to the whole imaged volume (Extended Data Fig. 9a). Second, the imaged volume was binned in quadrants using a 10 by 10 grid, and a new receptive field centre was fit to individual quadrants; these fits were constrained to be within 60° in azimuth and 35° in elevation from the global preferred retinotopic location. Receptive field centres from each quadrant were combined into a coarse retinotopic map, which was finally interpolated to the full pixel size of the FOV and smoothed with a 50-μm Gaussian. The retinotopic map was used to assign wide-field receptive field centres to each neuron on the basis of their position in the FOV. Retinotopic maps were also used to confirm the targeting of the experiment to V1, and discard cortical territories in higher visual areas from further analysis.

Linear neuronal receptive fields were estimated by reverse-correlating the neuronal responses and the stimuli (Extended Data Fig. 9d). The regression problem was solved by a cross-validated, regularized pseudoinverse algorithm, which imposed that the Laplacian of the receptive field ($L = \nabla^2 F$) be close to zero at each point:

$$\begin{bmatrix} S \\ \lambda L \end{bmatrix} F = \begin{bmatrix} r \\ 0 \end{bmatrix}.$$

The regularization parameter λ sets the balance between the 2D smoothness of the receptive field and the prediction of the response (r) to the stimulus (S). For each receptive field, we used sixfold cross-validation to choose the regularization parameter λ that maximized the receptive field predictive performance. The receptive field performance was measured as the correlation between the predicted response and the data. For each neuron, we repeated three rounds of receptive field fitting to estimate the 'on' subfield, the 'off' subfield, and the subfield responding to absolute changes in luminance. On subfields were fit using only the white squares presentations as predictors. Off subfields were fit using only the black squares presentations as predictors. Absolute subfields were fit using the full stream of stimuli as predictors. Receptive field subfields were considered significant if their performance was >0.2 . The receptive field centre for each neuron was calculated as the weighted sum of its significant subfields.

Orientation tuning and retinotopic alignment of presynaptic ensembles

We used several statistical tests to ascertain whether the tuning of presynaptic ensemble accorded with that of the postsynaptic neuron. First, significant variations in angular counts of presynaptic preferred orientation were assayed with a two-sided, one-way Kruskal–Wallis test. Second, angular counts of presynaptic preferred and opposite

direction were compared with a two-tailed Wilcoxon signed-rank test. Third, circular correlation was used to ascertain whether the average preferred orientation of presynaptic ensembles correlated with that of the postsynaptic neurons. As a further test of alignment, the circular V statistic was used to assess whether the difference between the presynaptic and postsynaptic preferred orientation formed a unimodal circular distribution centred at 0°. Finally, the circular variance of the presynaptic direction preferences was used to measure the tuning of the presynaptic ensemble.

As an internal control for each experiment, the same analyses were repeated on 10^4 surrogate distributions drawn randomly from other simultaneously recorded neurons. To obtain an empirical P -value (P_{rand}) for this control, the statistics from the presynaptic ensembles were tested against a null distribution computed from the surrogate ensembles. These analyses were performed either by including all presynaptic neurons, or by splitting them by layer on the basis of cortical depths. Surrogate distributions were generated accordingly.

The axis of presynaptic spatial patterns was measured as the sum of the angular positions of presynaptic neurons around the postsynaptic neuron. The alignment between the angle of the presynaptic axis and the orientation selectivity of the postsynaptic neuron was tested with circular correlation and circular V test, with analyses equivalent to those used for orientation preference. To craft surrogate retinotopic ensembles matched in size and spatial scale, each cortical distribution of presynaptic neurons was modelled as a 2D isotropic Gaussian. Surrogate ensembles drawn from these fits were isotropic in cortical space by design, and once transformed into visual space, reflected and controlled for biases due to local inhomogeneity or a varying magnification factor in the retinotopic map.

The presynaptic spatial angular distributions were modelled as

$$A(x) = a \times \sin\left(\frac{\pi}{2} + 2x\right) + b \times N(\pi, \sigma^2) + c,$$

in which the density A of presynaptic neurons in each angular bin x around the postsynaptic neuron was the sum of a sinusoidal function aligned to the postsynaptic preferred orientation and a Gaussian function aligned to the postsynaptic anti-preferred direction.

To average the excitatory and inhibitory presynaptic densities measured in each experiment, we rotated them, aligned them and scaled them to a common template in which the preferred direction of the postsynaptic neuron pointed rightwards. Rotation was designed to align the preferred direction of the postsynaptic cell to 0° in visual space. Scaling was tailored to match in size symmetric Gaussian fits to the density of the inhibitory ensembles.

To estimate the direction selectivity of the postsynaptic neuron from the distribution of excitatory and inhibitory presynaptic ensembles, we used

$$DSI_{\text{est}} = \frac{(E_o - I_a) - (E_o - I_a)}{(E_o + I_a) + (E_o + I_a)},$$

in which E_o and I_a are the densities of excitatory and inhibitory presynaptic neurons in the angular sector opposite the preferred direction, and E_a and I_a are densities for the angular sector ahead.

Circular statistics were computed using the CircStat toolbox⁶⁷.

Statistics and reproducibility

We present results obtained from $n=17$ independent replicates of the same experiment. P values are summarized as: NS, not significant; * $P \leq 0.05$; ** $P \leq 0.01$; *** $P \leq 0.001$.

Reporting summary

Further information on research design is available in the Nature Research Reporting Summary linked to this paper.

Data availability

Source data for the figures are deposited at <https://github.com/lfedros/Rossi-et-al-2020>. All other relevant data are available from the corresponding author upon reasonable request.

Code availability

Code used in this study is deposited at <https://github.com/lfedros/Rossi-et-al-2020>.

47. Madisen, L. et al. Transgenic mice for intersectional targeting of neural sensors and effectors with high specificity and performance. *Neuron* **85**, 942–958 (2015).
48. Wechselblatt, J. B., Flister, E. D., Piscopo, D. M. & Niell, C. M. Large-scale imaging of cortical dynamics during sensory perception and behavior. *J. Neurophysiol.* **115**, 2852–2866 (2016).
49. Gorski, J. A. et al. Cortical excitatory neurons and glia, but not GABAergic neurons, are produced in the Emx1-expressing lineage. *J. Neurosci.* **22**, 6309–6314 (2002).
50. Mayford, M. et al. Control of memory formation through regulated expression of a CaMKII transgene. *Science* **274**, 1678–1683 (1996).
51. Peron, S. P., Freeman, J., Iyer, V., Guo, C. & Svoboda, K. A cellular resolution map of barrel cortex activity during tactile behavior. *Neuron* **86**, 783–799 (2015).
52. Wickersham, I. R., Finke, S., Conzelmann, K. K. & Callaway, E. M. Retrograde neuronal tracing with a deletion-mutant rabies virus. *Nat. Methods* **4**, 47–49 (2007).
53. Marshel, J. H., Mori, T., Nielsen, K. J. & Callaway, E. M. Targeting single neuronal networks for gene expression and cell labeling in vivo. *Neuron* **67**, 562–574 (2010).
54. Rancz, E. A. et al. Transfection via whole-cell recording *in vivo*: bridging single-cell physiology, genetics and connectomics. *Nat. Neurosci.* **14**, 527–532 (2011).
55. Osakada, F. et al. New rabies virus variants for monitoring and manipulating activity and gene expression in defined neural circuits. *Neuron* **71**, 617–631 (2011).
56. Goldey, G. J. et al. Removable cranial windows for long-term imaging in awake mice. *Nat. Protocols* **9**, 2515–2538 (2014).
57. Judkewitz, B., Rizzi, M., Kitamura, K. & Häusser, M. Targeted single-cell electroporation of mammalian neurons *in vivo*. *Nat. Protocols* **4**, 862–869 (2009).
58. Kitamura, K., Judkewitz, B., Kano, M., Denk, W. & Häusser, M. Targeted patch-clamp recordings and single-cell electroporation of unlabeled neurons *in vivo*. *Nat. Methods* **5**, 61–67 (2008).
59. Pologruto, T. A., Sabatini, B. L. & Svoboda, K. ScanImage: flexible software for operating laser scanning microscopes. *Biomed. Eng. Online* **2**, 13 (2003).
60. Kim, E. J., Jacobs, M. W., Ito-Cole, T. & Callaway, E. M. Improved monosynaptic neural circuit tracing using engineered rabies virus glycoproteins. *Cell Rep.* **15**, 692–699 (2016).
61. Drobizhev, M., Makarov, N. S., Tilro, S. E., Hughes, T. E. & Rebane, A. Two-photon absorption properties of fluorescent proteins. *Nat. Methods* **8**, 393–399 (2011).
62. Brondum, M., Sato, S. S., Rossi, L. F., Ferrara, S. & Ratto, G. M. Finding a needle in a haystack: identification of EGFP tagged neurons during calcium imaging by means of two-photon spectral separation. *Front. Mol. Neurosci.* **5**, 96 (2012).
63. Kleiner, M. et al. What's new in psychtoolbox-3. *Perception* **36**, 1–16 (2007).
64. Burgess, C. P. et al. High-yield methods for accurate two-alternative visual psychophysics in head-fixed mice. *Cell Rep.* **20**, 2513–2524 (2017).
65. Pachitariu, M. et al. Suite2p beyond 10,000 neurons with standard two-photon microscopy. Preprint at <https://doi.org/10.1101/061507> (2016).
66. Dipoppa, M. et al. Vision and locomotion shape the interactions between neuron types in mouse visual cortex. *Neuron* **98**, 602–615 (2018).
67. Berens, P. CircStat: a MATLAB toolbox for circular statistics. *J. Stat. Softw.* **31**, 1–21 (2009).

Acknowledgements We thank E. Callaway for sharing viruses via the Salk Institute Vector Core; M. Rizzi for advice on electroporation; M. Krumin for support with microscopy; C. Reddy for help with plasmid production; M. Drobizhev for providing the two-photon cross-section of fluorescent proteins; S. Bugeon for help with histology and anatomical registration; L. Mariotti for help with anatomical reconstructions and cell counting; M. Scanziani for suggestions on the manuscript; and K. Balint, S. Trenholm, B. Roska and M. Tripodi for advice and for genetic materials that we used in pilot studies. This work was supported by the Wellcome Trust (grant 099692 to L.F.R., and grants 205093 and 108726 to K.D.H. and M.C.). M.C. holds the GlaxoSmithKline/Fight for Sight Chair in Visual Neuroscience.

Author contributions L.F.R., K.D.H. and M.C. conceived the experiments. L.F.R. refined the techniques, performed the experiments and analysed the data. L.F.R., K.D.H. and M.C. wrote the paper.

Competing interests The authors declare no competing interests.

Additional information

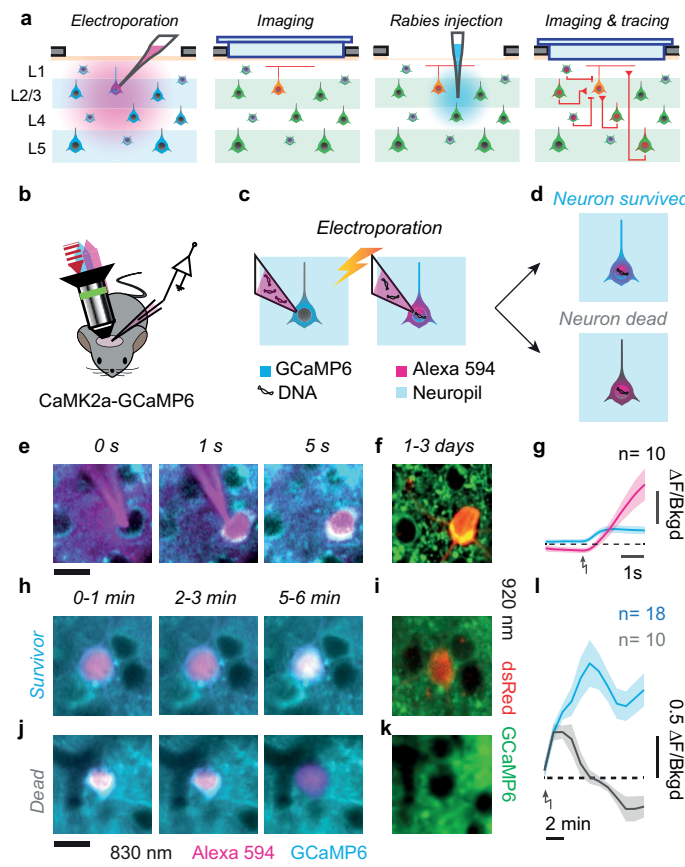
Supplementary information is available for this paper at <https://doi.org/10.1038/s41586-020-2894-4>.

Correspondence and requests for materials should be addressed to L.F.R.

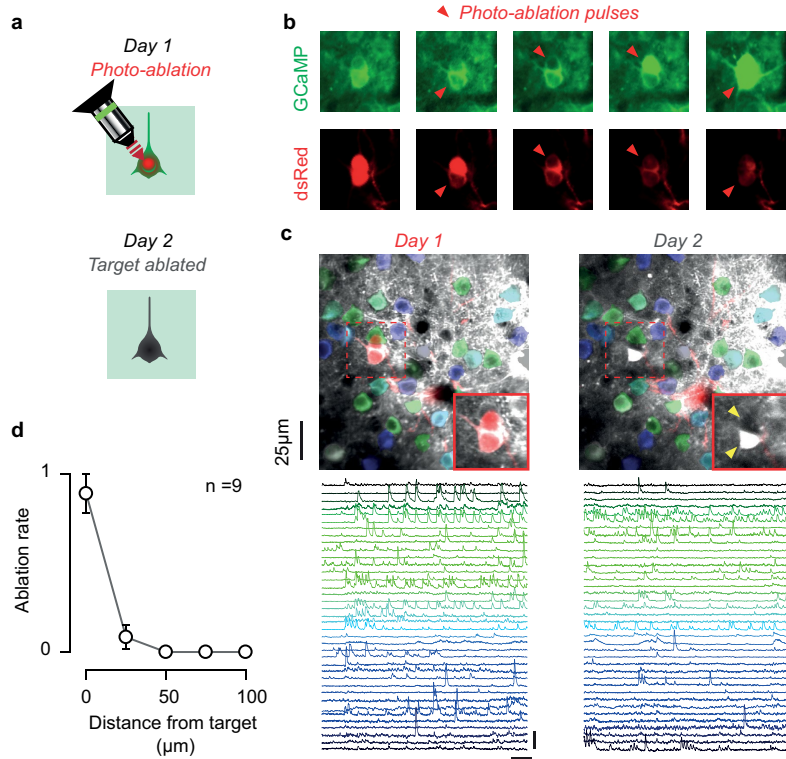
Peer review information *Nature* thanks Hillel Adesnik and the other, anonymous, reviewer(s) for their contribution to the peer review of this work.

Reprints and permissions information is available at <http://www.nature.com/reprints>.

Article

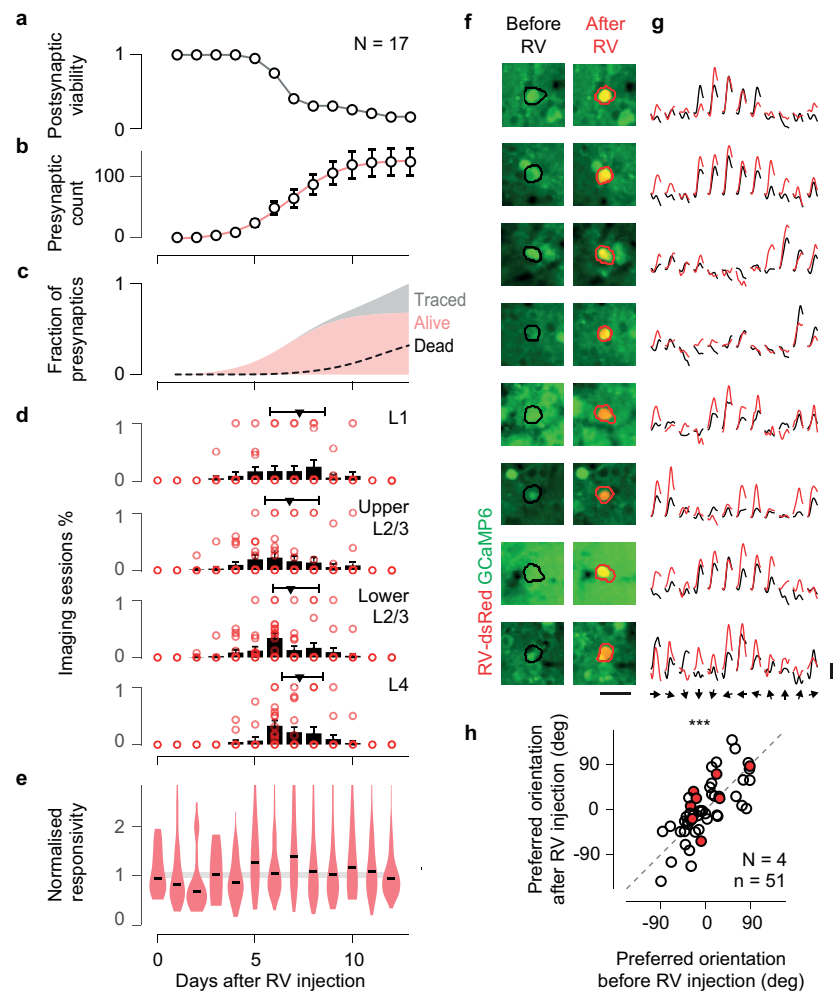


Extended Data Fig. 1 | Targeted single-neuron electroporation with survival control in vivo. **a**, Experimental pipeline: electroporation of the postsynaptic neuron, targeted by shadow-imaging and expression of GCaMP6; imaging of the postsynaptic neuron, labelled by dsRed; injection of the modified rabies virus; imaging and tracing of the presynaptic neurons marked by dsRed. **b–d**, Schematic of the electroporation technique, performed under a two-photon microscope on a transgenic mouse expressing GCaMP6 in cortical excitatory neurons. **b**, A pipette filled with DNA plasmids and Alexa Fluor 594 is targeted to a craniotomy; an 820-nm laser (red) excites Alexa Fluor 594 fluorescence (magenta) and GCaMP6 fluorescence (cyan). The latter is insensitive to neural activity because 820 nm is an isosbestic wavelength, at which calcium-bound and calcium-free isoforms fluoresce approximately equally. **c**, Upon electroporation, DNA plasmids and Alexa Fluor 594 are transferred into a neuron expressing GCaMP6. **d**, A healthy neuron maintains its GCaMP6 concentration and the resulting calcium-insensitive fluorescence (top), whereas a neuron with a damaged membrane bleeds indicator, gradually darkening and disappearing against the surrounding neuropil (bottom). **e**, Time lapse of an electroporation in layer 2/3 of mouse V1, using Alexa Fluor 594 negative contrast and calcium-insensitive GCaMP6 fluorescence imaging: approach (left), electroporation (middle) and pipette withdrawal (right). **f**, The same neuron as in **e**, imaged the next 1–3 days at 920 nm, expressing the electroporated genes for dsRed (red) and maintaining healthy GCaMP6 expression (green). **g**, Average fluorescence ($\text{mean} \pm \text{s.e.m.}$) of somatic Alexa Fluor 594 (magenta) and GCaMP6 (cyan), relative to neuropil background (dashed line represents unity) before and after electroporation (arrow, $n=10$ neurons). **h, i**, As in **e, f**, but with a slower time lapse of a neuron that survived the procedure. Images in **h** are 30-s-long averages acquired 0–1 min (left), 2–3 min (centre) and 5–6 min (right) after electroporation. **j, k**, As in **h, i**, for a neuron that did not recover from the electroporation. **l**, As in **g**, for GCaMP6 somatic fluorescence ($\text{mean} \pm \text{s.e.m.}$) in neurons that did (cyan, $n=18$) or did not (grey, $n=10$) survive the procedure. Scale bar, 15 μm (for all fluorescence images).



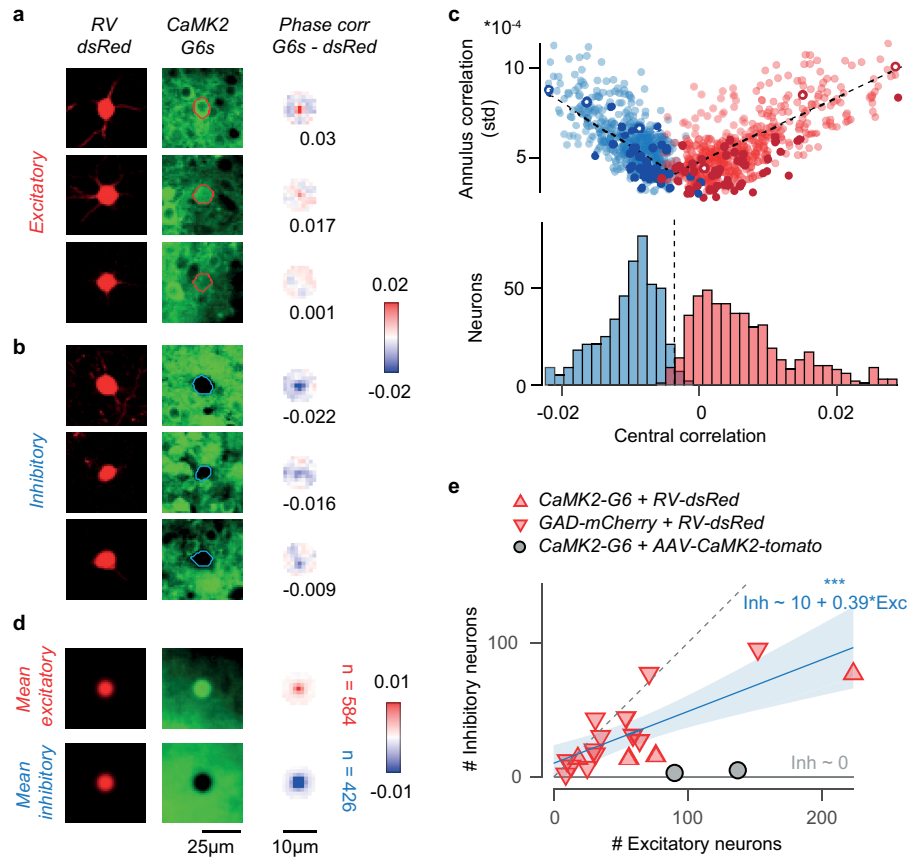
Extended Data Fig. 2 | Photo-ablation of supernumerary postsynaptic neurons before rabies injection. **a**, Cartoon of the protocol. The target neuron expresses both GCaMP6 (green) and dsRed (red), whereas surrounding neurons express only GCaMP6. The day after electroporation (day 1), the neuron is targeted with steady two-photon illumination at 820 nm, focused with intensity of approximately 150 mW, for 10–20 s (top). The target neuron is ablated and by the next day (day 2) it has disappeared (bottom). **b**, Time-lapse imaging during the photo-ablation of two neighbouring neurons, lasting approximately 10 min. Imaging at 920 nm shows calcium-sensitive fluorescence of GCaMP6 (top) and fluorescence of dsRed (bottom). Each of the neurons was targeted with two photo-ablation pulses (red triangles). Photo-ablation pulses lasted 20 s, and each neuron was imaged for 30 s

afterwards. Each pulse increases cellular damage: localized photo-bleaching after the first pulse; elevated intracellular calcium and cell swelling after the second pulse. Neighbouring cells, not expressing dsRed, resist the photo-damage. **c**, The successful elimination of the target neurons (red, see insets) is confirmed the day following the photo-ablation procedure: by day 2, the target neuron has either disappeared (yellow arrow, top neuron) or gone in apoptosis (yellow arrow, bottom neuron). The surrounding tissue is unaffected, as shown by the normal activity detected in neighbouring neurons using Suite2p (blue-green ROIs and traces; scale bar, 30 s and 10 s.d.). **d**, Effectiveness of photo-ablation as a function of cortical distance from the photo-ablation target neuron ($n = 9$ attempts, mean \pm s.e.m.).


Extended Data Fig. 3 | Time course of rabies tracing and recordings.

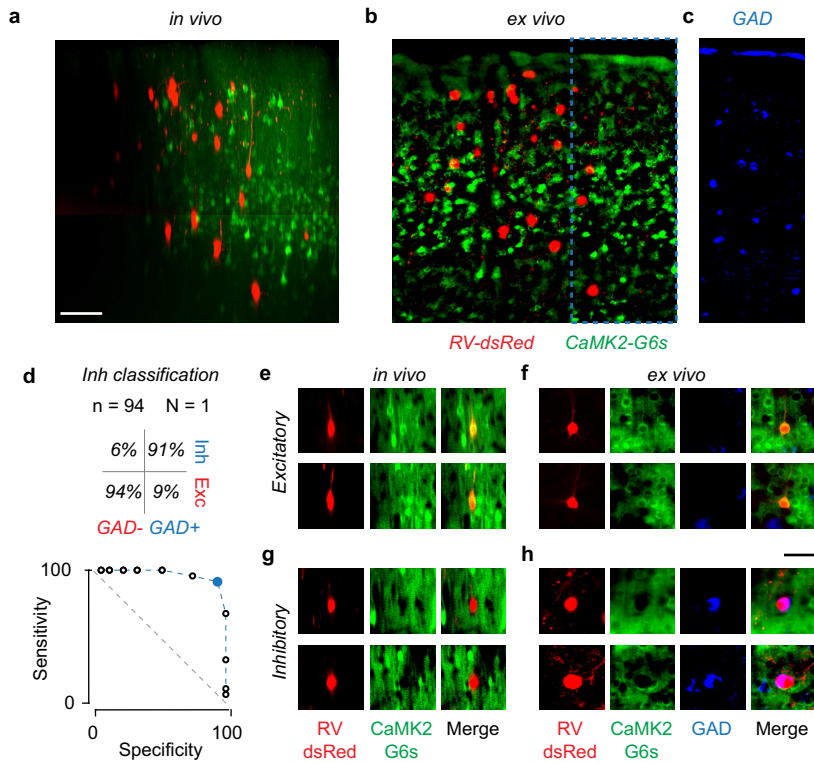
a, Viability of postsynaptic neurons as a function of day after the rabies virus injection, based on $n=17$ injections. **b**, Count of observed presynaptic neurons traced over the same period from $n=17$ postsynaptic neurons (mean \pm s.e.m.). **c**, Fraction of viable presynaptic neurons (red) over the total traced (grey), and worst-case-scenario population mortality of presynaptic neurons (dashed), estimated assuming the viability of each newly labelled presynaptic neuron degrades at the same rate as the viability of the postsynaptic neurons measured in **a**. **d**, Average distribution across mice ($n=17$, mean \pm s.e.m.) of the imaging sessions used to record the responses of presynaptic neurons, split by cortical layer. The time of imaging did not systematically change across layer (black triangle, median, first and third quartiles), and most of the data were acquired before presynaptic neurons suffered from the toxicity of the rabies virus. **e**, Distribution of responsivity of the presynaptic neurons across days

(red violin plot with black median). Responsivity was measured as the maximum average stimulus-triggered response. To compare across sessions, presynaptic responsivity was normalized to the median responsivity of the local population (shaded line). **f**, Longitudinal imaging of presynaptic neurons identified before (left, black ROI) and 5–12 days after (right, red ROI) rabies virus infection. Scale bar, 25 μ m. **g**, Average responses to drifting gratings of the same presynaptic neurons before (black) and after (red) the rabies virus infection. Responses (4-s long) were z-scored with respect to blank trials. Scale bar, 1 s.d. **h**, Preferred orientation of presynaptic neurons recorded before and after the rabies virus infection. At the time of recording used in this study, the preferred orientation of presynaptic neurons is unperturbed by the rabies virus infection ($n=51$ neurons from $n=4$ mice, circular correlation 0.76, $P_r = 1.6 \times 10^{-6}$, Ztest).



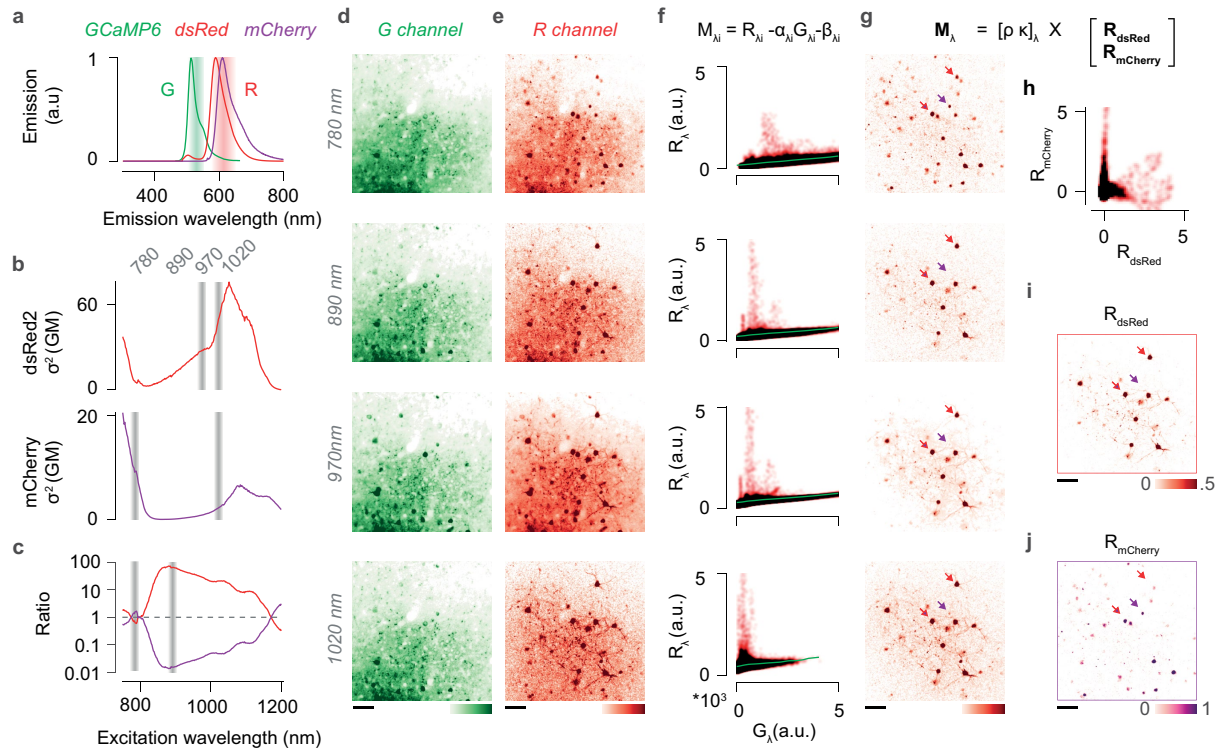
Extended Data Fig. 4 | Classification of excitatory and inhibitory presynaptic neurons. **a**, Three example excitatory presynaptic neurons showing similar expression of dsRed (left) and decreasing expression of GCaMP6 (middle). The somatic masks obtained from dsRed and the GCaMP6 signal were used to compute a map of phase correlation in the 5- μ m-radius annulus around the somatic centre (right). In the first two examples, the stronger GCaMP6 expression in the soma compared to the surrounding neuropil results in positive peaks of the phase correlation. **b**, As in **a**, for three example inhibitory neurons. The lack of GCaMP6 expression in the soma results in negative peaks of the phase correlation. **c**, For each presynaptic neuron, the central peak of phase correlation is plotted against the s.d. of the phase correlation within the 5- μ m annulus centred on the soma (top). Darker dots indicate neurons the identity of which was confirmed by immunostaining. Open dots represent example neurons shown in **a**, **b**. A classification boundary was used to split the clusters of excitatory (red) and inhibitory neurons (blue). This boundary was identified independently for each presynaptic ensemble

with a bilinear fit. The average fit across datasets is shown (black line). The histogram (bottom) summarizes the classification across experiments, with the average classification boundary. **d**, Average expression of dsRed (left), GCaMP6 (middle) and map of phase correlation (right) for presynaptic neurons classified as excitatory neurons (top, $n = 584$) or inhibitory neurons (bottom, $n = 426$). **e**, Number of presynaptic neurons classified as inhibitory versus excitatory in experiments in *CaMK2a-GCaMP6* mice (red upward triangles, $n = 13$) and *GAD2-NLS-mCherry* mice (red downward triangles, $n = 4$). A linear fit (blue, $r = 0.6, P = 2.6 \times 10^{-3}$, linear correlation, *F*-test) shows that the fraction of traced presynaptic neurons that are inhibitory tends towards 30% as the yield of tracing increases; yet, owing to the positive intercept, the fraction of inhibitory neurons may appear as high as 60% in experiments with low tracing yield. In control experiments in which the red marker *tdTomato* was expressed only in excitatory neurons (*AAV-CaMK2-tomato* in *CaMK2a-GCaMP6* mice, grey circles), the fraction of neurons incorrectly classified as inhibitory was below 5%.



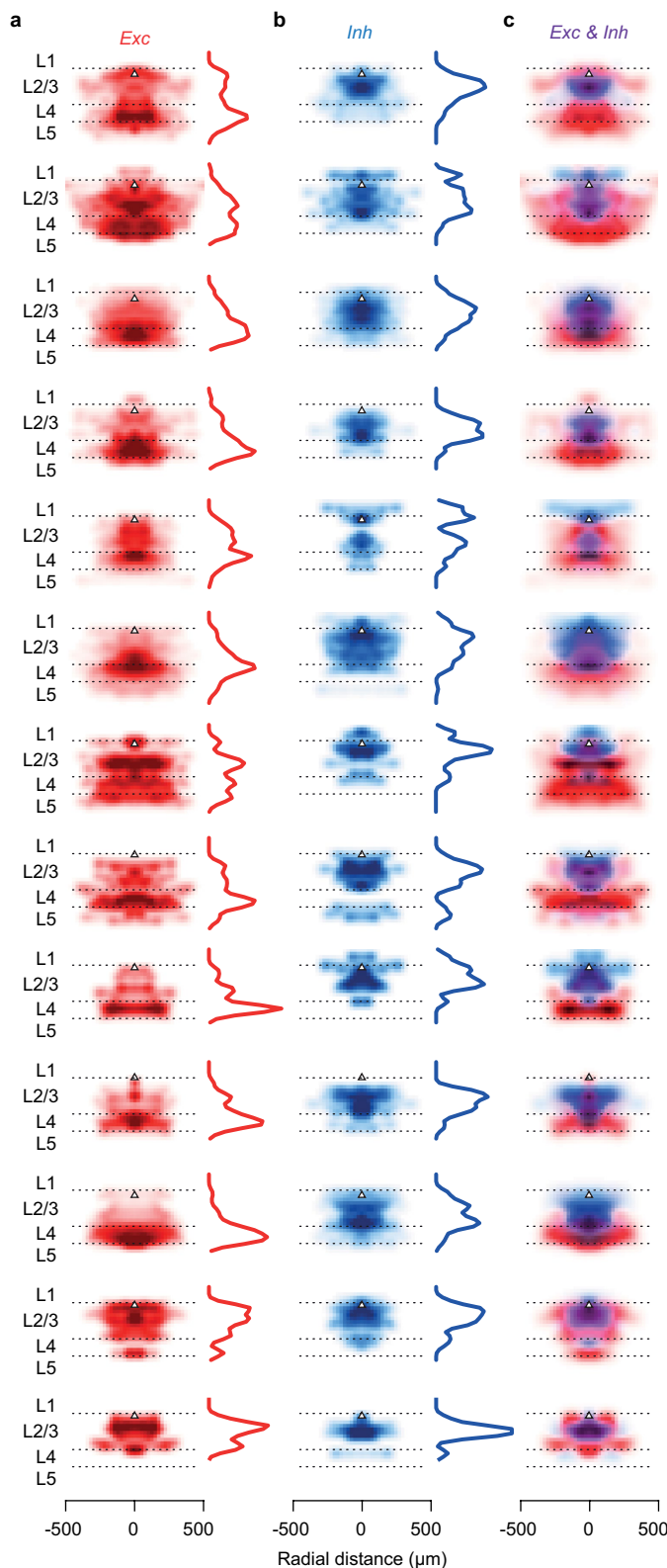
Extended Data Fig. 5 | Immunohistochemical verification of presynaptic neuron classification method. **a**, Coronal maximum projection from a z-stack acquired *in vivo*, showing a section through a presynaptic network labelled with RV-dsRed (red) in a *CaMK2a–GCaMP6s* transgenic mouse (green). Scale bar, 50 μm . **b**, Coronal brain slice matching the section in **a**. We could match $n = 94$ out of the $n = 105$ neurons traced *in vivo*. **c**, Inset from **b** (dashed) showing the immunostaining for the inhibitory neurons marker GAD (blue). **d**, ROC curve illustrating the sensitivity and specificity of the neuron classification method based on somatic GCaMP6 fluorescence (Extended Data Fig. 4) against

the ground-truth measurements obtained by immunostaining against GAD, for a range of classification boundaries. The fitted classification boundary was optimal (blue dot), yielding a specificity of 94% and sensitivity of 91%. **e**, Two example presynaptic neurons classified as excitatory ($n = 49$) from the z-stack in **a**. **f**, Slice immunostaining of the two neurons in **e**. Neurons were confirmed as excitatory if they expressed GCaMP6 and were GAD-negative ($n = 45$). Scale bar, 40 μm . **g**, As in **e**, **f**, for two example presynaptic neurons classified as inhibitory. Neurons were confirmed as inhibitory if they did not express GCaMP6 and were GAD-positive ($n = 42$).



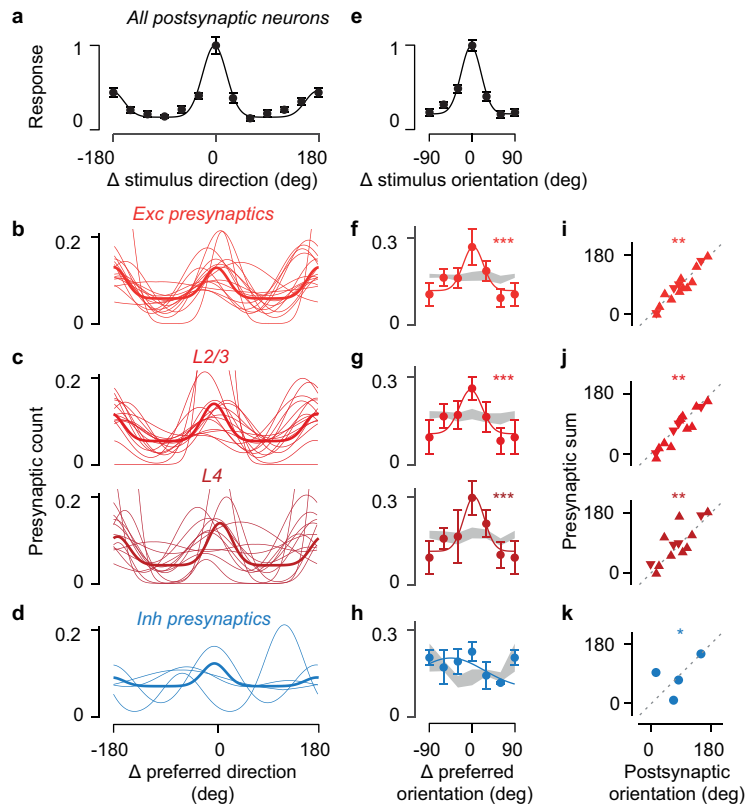
Extended Data Fig. 6 | Spectral unmixing of dsRed and mCherry fluorescence. **a**, Emission spectra of GCaMP6, dsRed and mCherry. Shaded areas indicate the emission band captured by the green (G) and red (R) channels of the microscope. The G channel collects mostly GCaMP6 fluorescence, and the R channel captures a mixture of mCherry, dsRed and GCaMP6 fluorescence. Emission spectra were normalized to their peak. **b**, Two-photon action cross-section of dsRed (top, red) and mCherry (bottom, purple). **c**, Ratio between the two-photon action cross-sections of dsRed and mCherry (red) and its inverse (purple). Shaded bands in **b**, **c** indicate the excitation wavelengths used for imaging: 780, 890, 970 and 1,020 nm. The four wavelengths were chosen to maximize the SNR of each fluorophore while ensuring the ratio between the two signals was maximal. **d**, Example field of view imaged at the four excitation wavelengths in the G channel. GCaMP6 was expressed in all neurons with an AAV2.1-Syn-GCaMP6s in a GAD-NLS-mCherry mouse; a subset of presynaptic neurons was traced with a dsRed rabies virus. **e**, As in **d**, for the R

channel. **f**, The fluorescence in the R channel (R_λ) plotted against the fluorescence in the G channel (G_λ) for each pixel, and for each excitation wavelength λ . Because the GCaMP6 labelling was dense and both the dsRed and the mCherry signals were sparse, and because the contribution of dsRed and mCherry to G_λ was minimal, the GCaMP6 signal contributing to R_λ could be recovered by piecewise robust linear regression ($\alpha G_\lambda + \beta$). **g**, The image representing the linear mix of dsRed or mCherry signals, M_λ , was recovered by subtracting the scaled G_λ from the R_λ . **h**, An iterative algorithm was used to linearly unmix the two source images. Each unmixing iteration was constrained to minimize the quadratic reconstruction error over the data and return maximally uncorrelated sources R_{dsRed} and $R_{mCherry}$. **i,j**, The two source images R_{dsRed} and $R_{mCherry}$ for the example field of view in **d**, **e**. The unmixing procedure correctly recovers the nuclear localization of mCherry without any prior. Scale bars, 50 μm . Similar results were obtained for all GAD-NLS-mCherry mice ($n=4$).



Extended Data Fig. 7 | Distributions of individual excitatory and inhibitory presynaptic ensembles. **a**, Density of excitatory presynaptic neurons around the postsynaptic neuron (black triangle) as a function of cortical depth and radial distance from the postsynaptic neuron. Density was normalized to its maximum for display purposes. Depth marginals are shown on the left of each

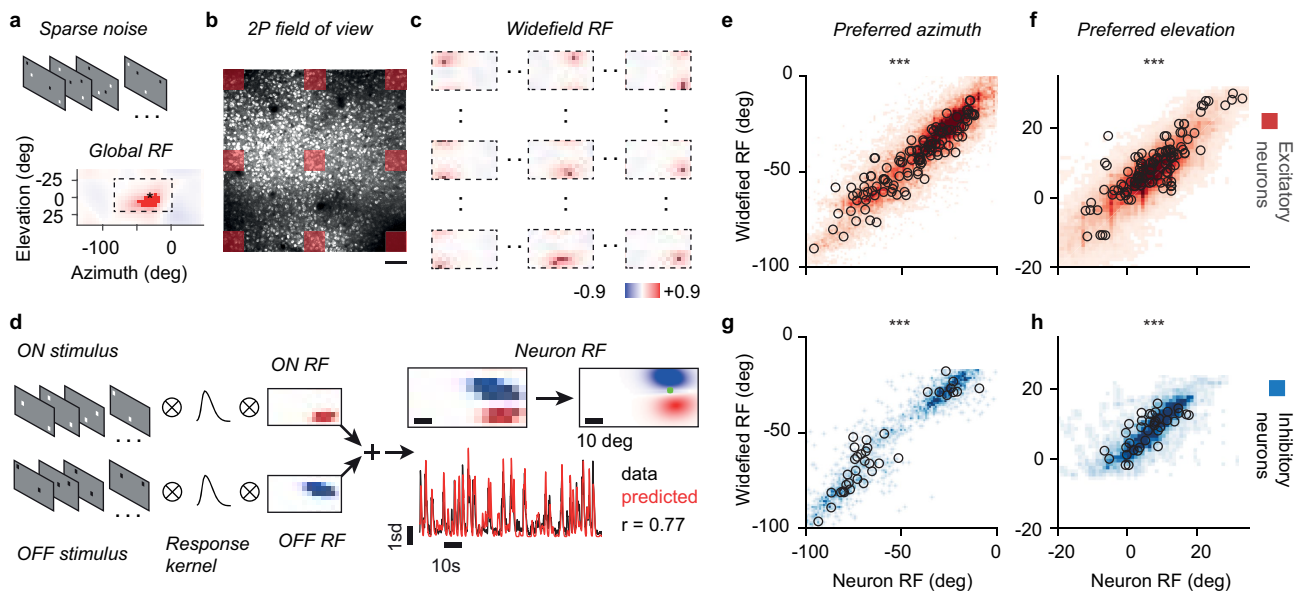
density map. **b**, As in **a**, for inhibitory presynaptic neurons. **c**, Overlay of excitatory and inhibitory densities shown in **a**, **b**. Hue indicates the relative proportion of excitatory (red) and inhibitory (blue) inputs, and saturation indicates maximum normalized neuronal density. Data are shown for the 13 experiments that included substantial recordings from L4.



Extended Data Fig. 8 | L2/3 neurons receive presynaptic excitation preferentially tuned to their orientation preference. **a**, Average tuning across the postsynaptic neurons responding to drifting gratings ($n=16$, mean \pm s.e.m.), after alignment of their preferred stimulus direction. **b**, Distribution of preferred direction relative to the postsynaptic preferred direction, for excitatory presynaptic ensembles across all layers ($n=15$, median \pm m.a.d.). **c**, As in b, for excitatory presynaptic ensembles within L2/3 (top) and within L4 (bottom). **d**, As in b, for inhibitory presynaptic ensembles. **e**, Average orientation tuning across the postsynaptic neurons responding to drifting gratings ($n=16$, mean \pm s.e.m.), after alignment of their preferred stimulus orientation. **f**, Average distribution of preferred orientation relative to the postsynaptic preferred orientation, for excitatory presynaptic neurons pooled across all layers ($n=15$, median \pm m.a.d.). Presynaptic ensembles tuning for orientation ($P_{\text{KW}} = 5 \times 10^{-8}$, two-sided one-way Kruskal-Wallis test) was significantly stronger than expected from random samples of the surrounding population (grey, median \pm m.a.d.). **g**, As in f, for presynaptic ensembles within L2/3 (top, $n=15$, $P_{\text{KW}} = 10^{-7}$) and within L4 (bottom, $n=13$, $P_{\text{KW}} = 2 \times 10^{-5}$). **h**, As in f, for inhibitory presynaptic ensembles ($n=4$). **i**, The tuning of the distributions of preferred orientation of excitatory presynaptic ensembles across layers plotted against the preferred orientation of their postsynaptic neuron. The co-tuning for orientation ($r = 0.75$, circular correlation, $P_r = 4 \times 10^{-3}$, Z-test; $P_V = 9 \times 10^{-8}$ circular V-test) was stronger than expected from random samples of the local population ($P_{r,\text{rand}} < 10^{-4}$ for circular correlation, $P_{V,\text{rand}} < 10^{-4}$ for V statistic). Upwards triangles represent experiments in *CaMK2α-GCaMP6* mice ($n=11$); downward triangles indicate experiments in *GAD2-NLS-mCherry* mice ($n=4$). **j**, As in i, for excitatory presynaptic ensembles within L2/3 (top, $r = 0.92$, $P_r = 5 \times 10^{-3}$, $P_V = 10^{-5}$, $P_{r,\text{rand}} = 2 \times 10^{-4}$, $P_{V,\text{rand}} < 10^{-4}$, $n = 15$) and within L4 (bottom, $r = 0.76$, $P_r = 2 \times 10^{-2}$, $P_V = 3 \times 10^{-3}$, $P_{r,\text{rand}} = 0.18$, $P_{V,\text{rand}} = 3 \times 10^{-3}$, $n = 13$). **k**, As in i, for inhibitory presynaptic ensembles. Inhibitory presynaptic ensembles were weakly biased to the orientation preference of the postsynaptic neuron ($P_V = 0.05$, circular V-test, $n = 4$).

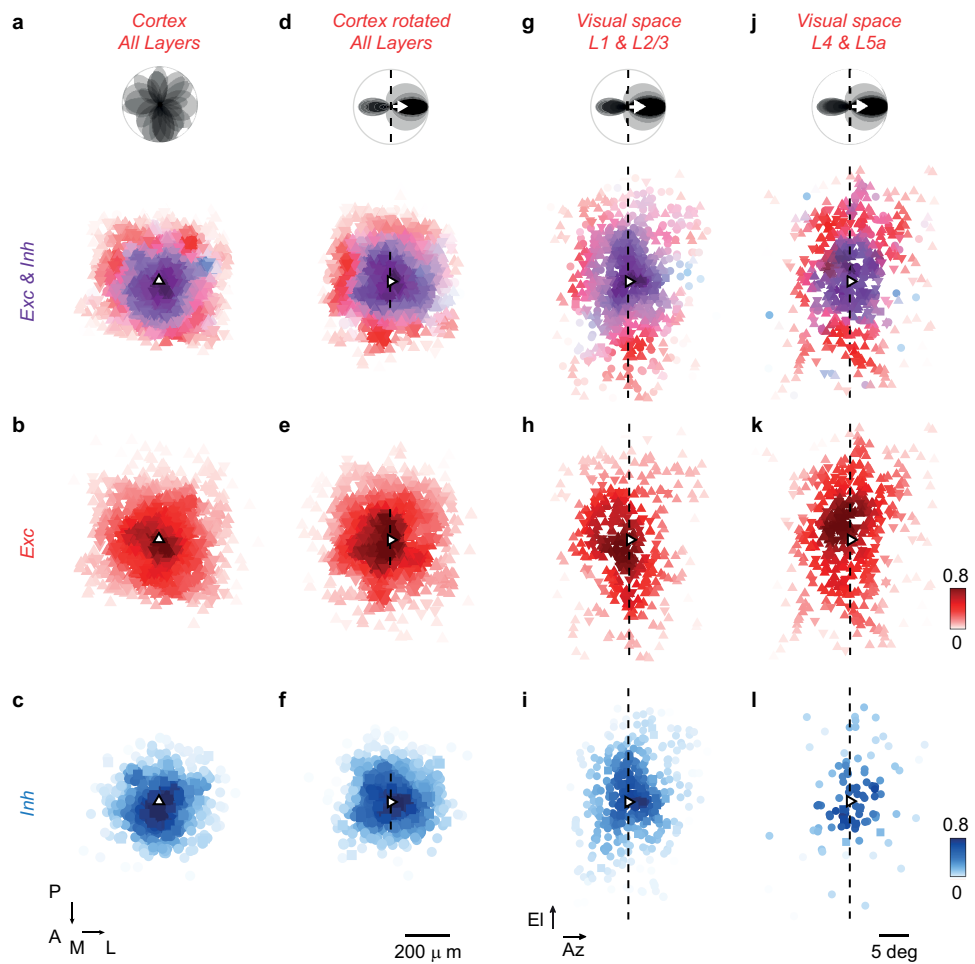
L2/3 (top, $n=15$, $P_{\text{KW}} = 10^{-7}$) and within L4 (bottom, $n=13$, $P_{\text{KW}} = 2 \times 10^{-5}$). **h**, As in f, for inhibitory presynaptic ensembles ($n=4$). **i**, The tuning of the distributions of preferred orientation of excitatory presynaptic ensembles across layers plotted against the preferred orientation of their postsynaptic neuron. The co-tuning for orientation ($r = 0.75$, circular correlation, $P_r = 4 \times 10^{-3}$, Z-test; $P_V = 9 \times 10^{-8}$ circular V-test) was stronger than expected from random samples of the local population ($P_{r,\text{rand}} < 10^{-4}$ for circular correlation, $P_{V,\text{rand}} < 10^{-4}$ for V statistic). Upwards triangles represent experiments in *CaMK2α-GCaMP6* mice ($n=11$); downward triangles indicate experiments in *GAD2-NLS-mCherry* mice ($n=4$). **j**, As in i, for excitatory presynaptic ensembles within L2/3 (top, $r = 0.92$, $P_r = 5 \times 10^{-3}$, $P_V = 10^{-5}$, $P_{r,\text{rand}} = 2 \times 10^{-4}$, $P_{V,\text{rand}} < 10^{-4}$, $n = 15$) and within L4 (bottom, $r = 0.76$, $P_r = 2 \times 10^{-2}$, $P_V = 3 \times 10^{-3}$, $P_{r,\text{rand}} = 0.18$, $P_{V,\text{rand}} = 3 \times 10^{-3}$, $n = 13$). **k**, As in i, for inhibitory presynaptic ensembles. Inhibitory presynaptic ensembles were weakly biased to the orientation preference of the postsynaptic neuron ($P_V = 0.05$, circular V-test, $n = 4$).

Article



Extended Data Fig. 9 | Mapping retinotopy using individual neurons versus wide-field signals. **a**, The stimulus used for retinotopic mapping was a sparse random pattern of white and black squares on a grey background (top). The fluorescence time-course from the entire field of view was used to compute a global stimulus-triggered average response elicited by changes in luminance at each position. The centre of mass of this global receptive field (RF) was used to constrain the fits of wide field and neuronal receptive field to the appropriate retinotopic region (dashed rectangle). **b**, Maximal projection from an example field of view. In this example, the field of view was subsampled in a grid of 9×9 regions of interest (ROIs, red squares) to compute wide-field receptive fields. Scale bar, 100 μm . **c**, The wide-field receptive fields calculated for the ROIs in **b**, normalized to their maximum. The wide-field receptive field centres from the grid of ROIs were interpolated to estimate a retinotopic map, assigning a wide-field receptive field to each cortical location, whether it contained a responsive neuron, an unresponsive neuron or neuropil. **d**, Estimation of neuronal receptive fields. ON (red) and OFF (blue) receptive fields were

estimated by regularized smooth pseudoinverse regression using either streams of white (ON) or black stimuli (OFF) as predictors, and assuming a common response kernel across neurons. ON and OFF subfields were then combined to estimate the receptive field centre (green dot). Receptive fields were considered significant if the cross validated correlation coefficient between predicted (red trace) and actual response (black trace) was greater than 0.2. **e**, Azimuth of neuron receptive field centre versus wide-field receptive field centre for all excitatory presynaptic neurons (black dots, $n=113$, $r_{\text{pre}}=0.89$, $P_{r,\text{pre}}=2.8 \times 10^{-39}$, linear correlation, F -test) and surrounding excitatory neurons (red density, $n=25,677$, $r_{\text{all}}=0.88$, $P_{r,\text{all}}<10^{-308}$, linear correlation F -test) across experiments. **f**, As in **e** for elevation ($r_{\text{pre}}=0.80$, $P_{r,\text{pre}}=9 \times 10^{-27}$; $r_{\text{all}}=0.85$, $P_{r,\text{all}}<10^{-308}$). **g, h**, As in **e, f**, for inhibitory presynaptic neurons (black dots, $n=37$, $r_{\text{pre}}=0.92$, $P_{r,\text{pre}}=1.3 \times 10^{-15}$, for azimuth; $r_{\text{pre}}=0.71$, $P_{r,\text{pre}}=9.7 \times 10^{-7}$, for elevation) and all inhibitory neurons ($n=1,963$, $r_{\text{all}}=0.95$, $P_{r,\text{all}}<10^{-308}$, for azimuth; $r_{\text{all}}=0.74$, $P_{r,\text{all}}<10^{-308}$, for elevation).



Extended Data Fig. 10 | Spatial connectivity accords with direction

selectivity in cortex and across layers. **a**, Distribution of excitatory and inhibitory presynaptic neurons in cortex, pooled across experiments ($n=17$), and polar tuning curves for each postsynaptic neuron (top). The colour hue indicates the average fraction of local excitatory (red) or inhibitory (blue) presynaptic neurons; the colour saturation indicates the maximum normalized input density, averaged across experiments. **b, c**, As in **a**, plotting the excitatory and inhibitory presynaptic neurons separately. **d**, As in **a**, after rotating each presynaptic cortical distribution to align the postsynaptic preferred direction ($n=16$). The cortical angle of rotation, corresponding to the postsynaptic preferred direction, was calculated from the local retinotopic

gradient at the postsynaptic location. After the alignment, the postsynaptic preferred orientation approximately maps to a line at the postsynaptic location (dashed line). **e**, As in **d**, for excitatory presynaptic neurons. **f**, As in **d**, for inhibitory presynaptic neurons. **g**, As in **d**, for the distribution of L1 and L2/3 excitatory and inhibitory presynaptic neurons in visual space, pooled across experiments after alignment to the preferred direction across postsynaptic neurons ($n=16$). **h, i**, As in **g**, distinguishing between excitatory and inhibitory presynaptic neurons. **j–l**, As in **g–i**, for presynaptic neurons in L4 and in superficial L5. In all panels, upwards triangles and circles represent *CaMK2a–GCaMP6* datasets; downward triangles and squares indicate *GAD2–NLS–mCherry* datasets.

Reporting Summary

Nature Research wishes to improve the reproducibility of the work that we publish. This form provides structure for consistency and transparency in reporting. For further information on Nature Research policies, see our [Editorial Policies](#) and the [Editorial Policy Checklist](#).

Statistics

For all statistical analyses, confirm that the following items are present in the figure legend, table legend, main text, or Methods section.

n/a Confirmed

- The exact sample size (n) for each experimental group/condition, given as a discrete number and unit of measurement
- A statement on whether measurements were taken from distinct samples or whether the same sample was measured repeatedly
- The statistical test(s) used AND whether they are one- or two-sided
Only common tests should be described solely by name; describe more complex techniques in the Methods section.
- A description of all covariates tested
- A description of any assumptions or corrections, such as tests of normality and adjustment for multiple comparisons
- A full description of the statistical parameters including central tendency (e.g. means) or other basic estimates (e.g. regression coefficient) AND variation (e.g. standard deviation) or associated estimates of uncertainty (e.g. confidence intervals)
- For null hypothesis testing, the test statistic (e.g. F , t , r) with confidence intervals, effect sizes, degrees of freedom and P value noted
Give P values as exact values whenever suitable.
- For Bayesian analysis, information on the choice of priors and Markov chain Monte Carlo settings
- For hierarchical and complex designs, identification of the appropriate level for tests and full reporting of outcomes
- Estimates of effect sizes (e.g. Cohen's d , Pearson's r), indicating how they were calculated

Our web collection on [statistics for biologists](#) contains articles on many of the points above.

Software and code

Policy information about [availability of computer code](#)

Data collection ScanImage v4.2 & 3.8 (written in Matlab)
Psychtoolbox-3

Data analysis Custom code written in Matlab (9.3.0.823005, R2017b). The code needed to reproduce the manuscript figures will be deposited at: <https://github.com/lfedros/Rossi-et-al-2020>.
Other original code will be available upon reasonable request to the authors.
Suite2P toolbox for Matlab (13/06/2017 version, <https://github.com/cortex-lab/Suite2P>)
CircStat toolbox for Matlab (24/05/2019 version, <https://github.com/circstat/circstat-matlab>)

For manuscripts utilizing custom algorithms or software that are central to the research but not yet described in published literature, software must be made available to editors and reviewers. We strongly encourage code deposition in a community repository (e.g. GitHub). See the Nature Research [guidelines for submitting code & software](#) for further information.

Data

Policy information about [availability of data](#)

All manuscripts must include a [data availability statement](#). This statement should provide the following information, where applicable:

- Accession codes, unique identifiers, or web links for publicly available datasets
- A list of figures that have associated raw data
- A description of any restrictions on data availability

Source data needed to reproduce the manuscript figures will be deposited at <https://github.com/lfedros/Rossi-et-al-2020>. Other data will be available from the authors upon reasonable request.

Field-specific reporting

Please select the one below that is the best fit for your research. If you are not sure, read the appropriate sections before making your selection.

Life sciences Behavioural & social sciences Ecological, evolutionary & environmental sciences

For a reference copy of the document with all sections, see nature.com/documents/nr-reporting-summary-flat.pdf

Life sciences study design

All studies must disclose on these points even when the disclosure is negative.

Sample size	While we did not use statistical methods to pre-determine sample sizes, our sample sizes are similar to those reported in previous publications in the field (cfrrt: Velez-Fort et al., Neuron, 2014; Wertz et al., Science; 2015, Lien and Scanziani, Nature, 2018). Moreover, during the revision process, we performed additional experiments which strengthened our conclusions and increased the sample size by 30% compared to the initial version.
Data exclusions	As described in the main text or methods section, we did not exclude any data or experiment from our analysis.
Replication	As described in the text, the results are based on 17 independent replicates of the same experiment. To show the reproducibility of each finding, we provide multiple examples of individual experiments and matching summary plots across experiments. Due to experimental challenges and risk factors associated with the techniques demonstrated in our study, not all attempts at replication were successful: we estimate the success rate of our experimental pipeline to be between 30-70%.
Randomization	Our study did not contain experimental groups so randomization does not apply.
Blinding	Our study did not contain experimental groups so blinding does not apply.

Reporting for specific materials, systems and methods

We require information from authors about some types of materials, experimental systems and methods used in many studies. Here, indicate whether each material, system or method listed is relevant to your study. If you are not sure if a list item applies to your research, read the appropriate section before selecting a response.

Materials & experimental systems

- | | |
|-------------------------------------|---|
| n/a | Involved in the study |
| <input type="checkbox"/> | <input checked="" type="checkbox"/> Antibodies |
| <input checked="" type="checkbox"/> | <input type="checkbox"/> Eukaryotic cell lines |
| <input checked="" type="checkbox"/> | <input type="checkbox"/> Palaeontology and archaeology |
| <input type="checkbox"/> | <input checked="" type="checkbox"/> Animals and other organisms |
| <input checked="" type="checkbox"/> | <input type="checkbox"/> Human research participants |
| <input checked="" type="checkbox"/> | <input type="checkbox"/> Clinical data |
| <input checked="" type="checkbox"/> | <input type="checkbox"/> Dual use research of concern |

Methods

- | | |
|-------------------------------------|---|
| n/a | Involved in the study |
| <input checked="" type="checkbox"/> | <input type="checkbox"/> ChIP-seq |
| <input checked="" type="checkbox"/> | <input type="checkbox"/> Flow cytometry |
| <input checked="" type="checkbox"/> | <input type="checkbox"/> MRI-based neuroimaging |

Antibodies

Antibodies used

mouse anti-GAD67 primary antibody (Millipore MAB5406)
donkey anti-mouse IgG Alexa 647 conjugate secondary antibody (Merk Millipore, AP192SA6)

Validation

Mouse anti-GAD67 primary antibody (Millipore MAB5406)
This Anti-GAD Antibody, clone 1G10.2 is validated for use in IH, IH(P), WB for the detection of GAD67. This Anti GAD antibody has more than 75 product citations.
Key Applications include Immunohistochemistry, Immunohistochemistry (Paraffin), Western Blotting
Application Notes: Immunohistochemistry on 4% paraformaldehyde fixed mouse and rat tissue: 1:1,000-1:5,000. The antibody has also worked well on human tissue fixed for 10 minutes in 4% PFA at 4°C or 100% ethanol at +20°C or 100% acetone at -20°C at dilutions of 1:2,500-1:5,000. Optimal working dilutions must be determined by end user.
Donkey anti-mouse IgG Alexa 647 conjugate secondary antibody (Merk Millipore, AP192SA6)

Animals and other organisms

Policy information about [studies involving animals](#); [ARRIVE guidelines](#) recommended for reporting animal research

Laboratory animals

Experiments were performed on twenty 7-12 weeks old mice of both sexes, maintained on a 12 hours light/dark cycle, at 20-24°C and 45-65% humidity, in individually ventilated cages. Five mice were Camk2a-tTA; EMX1-Cre; TIGRE-Ins-TRE-LSL-GCaMP6f (Ai93D) triple transgenic mice, expressing the calcium indicator GCaMP6f in all cortical excitatory neurons. Six mice were Camk2a-tTA; EMX1-Cre; TIGRE-Ins-TRE-LSL-GCaMP6s (Ai94D) triple transgenic mice, expressing the calcium indicator GCaMP6fs in all cortical excitatory neurons. Five mice were Camk2a-tTA; tetO-GCamp6s double transgenic mice, expressing GCaMP6s in all cortical excitatory neurons. Transgenic mice were bred from the following parental lines: Emx1-IRES-Cre (Stock #005628, The Jackson Laboratory); CamK2a-tTA (Stock #007004); Ai93 (Stock #024103); Ai94 (Stock #024104); TRE-GCamp6f (Stock #024742). Four experiments involved Gad2-T2a-NLS-mCherry animals, expressing the far red fluorescent protein mCherry localised to the nucleus of inhibitory neurons (Stock #023140).

Wild animals

No wild animals were used in the study.

Field-collected samples

No field collected samples were used in the study.

Ethics oversight

All experimental procedures were conducted in accordance with the UK Animals Scientific Procedures Act (1986). Experiments were performed at University College London under personal and project licenses released by the Home Office following appropriate ethics review.

Note that full information on the approval of the study protocol must also be provided in the manuscript.